Migration of cells in a social context

Søren Vedel[a,1], Savaş Tay[b,1], Darius M. Johnston[c,d,e], Henrik Bruus[a], and Stephen R. Quake[c,d,e,2]

[a]Department of Micro- and Nanotechnology, Technical University of Denmark, DK-2800 Kongens Lyngby, Denmark; [b]Department of Biosystems Science and Engineering, ETH Zurich, 4058 Basel, Switzerland; and Departments of [c]Applied Physics and [d]Bioengineering and [e]Howard Hughes Medical Institute, Stanford University, Stanford, CA 94305

Edited by Robert H. Austin, Princeton University, Princeton, NJ, and approved November 15, 2012 (received for review March 13, 2012)

In multicellular organisms and complex ecosystems, cells migrate in a social context. Whereas this is essential for the basic processes of life, the influence of neighboring cells on the individual remains poorly understood. Previous work on isolated cells has observed a stereotypical migratory behavior characterized by short-time directional persistence with long-time random movement. We discovered a much richer dynamic in the social context, with significant variations in directionality, displacement, and speed, which are all modulated by local cell density. We developed a mathematical model based on the experimentally identified "cellular traffic rules" and basic physics that revealed that these emergent behaviors are caused by the interplay of single-cell properties and intercellular interactions, the latter being dominated by a pseudopod formation bias mediated by secreted chemicals and pseudopod collapse following collisions. The model demonstrates how aspects of complex biology can be explained by simple rules of physics and constitutes a rapid test bed for future studies of collective migration of individual cells.

cell migration | single-cell analysis | physical modeling | microfluidics

Collective migration, from migrating cells in tissue (1–3) to swarming insects (4) to flocks of birds (5) and pedestrians in heavy traffic (6), constitutes one of the most fascinating spectacles in nature. In addition to its aesthetic qualities, social cell migration is involved in embryonic development (7), wound healing (8), and immune response (9), and unregulated migration leads to disease, including cancer metastasis (10). Previous work on single-cell migration has focused on isolated (11–20) or strongly polarized and aligning (21, 22) cell types, mostly using population-averaged bulk assays (23) or simple observations in a social context (2, 3). However, strongly cross-correlated cell motion and collective substrate deformation has been found to arise in mechanically interlinked cells transmitting forces through both cell–cell linkages and the substrate (24–29). These studies revealed useful information on cell migration, but because in general the relevant interactions in a social context and their relative importance are not established, migratory behavior of cells in a social context remains as one of the major unresolved problems in biology (30). Furthermore, striking social effects such as highly sensitive collective responses in a number of sensing systems [e.g., quorum sensing (31, 32) and onset of collective behavior in *Dictyostelium discoideum* (33)] mediated by increased levels of cell-secreted signals in higher cell density indicate that mechanical links are not necessary for collective behavior. At the subcellular level, many types of nonswimming motile cells involved in multicellular biology [e.g., fibroblasts, *Dictyostelium*, and neutrophils (13, 14, 16–18)] have been found to transmit traction force to the substrate by intracellularly polymerizing their cytoskeletons in dynamically formed membrane protrusions known as pseudopodia. However, whether the social context changes this, mechanisms by which the social context manifests itself, and the implications of being close to neighboring cells all remain unexplored.

Here we shed light on these fundamental questions using a combination of high-throughput microfluidic cell culture (34) of 3T3 fibroblast cells expressing fluorescent fusion proteins, time-lapse microscopy with subcellular resolution, and physical modeling (*SI Appendix*, *Materials and Methods* and *Model Details*). Contrary to previous work (22, 24–26, 29), these cells form neither 2D sheets nor 3D structures, nor are they highly polarized, and their single-cell migratory behavior is established (13, 14, 16). The microfluidic cell culture platform hosts independent and isolated culture conditions in each of the isolated 96 polymethylsiloxane (PDMS) chambers (34-nL volume) that mimic physiological conditions more plausibly than traditional cell-culture environments in which concentrations of, for instance, secreted signaling molecules are diluted into large volumes of surrounding fluid. Using only freshly thawed cells, we cultured them at densities ranging from 15 to ∼100% confluence in up to 24 parallel chambers at a time; more than 8,000 cells were quantified, yielding hundreds of thousands of data points from a total of only five experimental runs. Experiments on any given density were repeated at least once on different chips, and we studied different densities in parallel on each chip (*SI Appendix*, Table S1). We replaced the chamber volume at time $t = 0$, sealed the chamber using the microfluidic membrane valves, and imaged the cells every 4–6 min for 5–6 h, focusing on a region of ∼500 μm × 700 μm in the center of the chamber to avoid edge effects, which contained a population consisting of between 36 and 246 cells [corresponding to an average minimum nucleus–nucleus distance $\bar{d}_{\min}$ in the range of approximately one to three cell diameters, which on average is 41.7 μm (*SI Appendix*, Fig. S12*A*)]. Using different fluorescent fusion proteins to image the nuclei (green) and cytosols (red) (Fig. 1*A*) coupled with high imaging resolution allowed us to track single-cell migration behavior and pseudopodia, producing a very comprehensive dataset; such detailed quantitative measurements of single-cell behavior are emerging as a strong tool for studying biological systems, as recently exemplified for cell cycle stability (35) and inflammatory signaling (36).

Results

Quantitative Cell Migration Characteristics. Our measurements reveal the migration characteristics of cells at different densities. Although all cells move (Fig. 1*A* and *SI Appendix*, Fig. S2 and Table S2 and Movie S1) with no preferred overall direction (*SI Appendix*, Fig. S3), we find large diversity with negligible cross-correlation in the migratory behavior of the cells at the same density (Figs. 1 and 2E and *SI Appendix*, Fig. S2): Some cells move along almost straight lines, other follow curved paths, and yet others traverse very short distances with little apparent directionality (Fig. 1*B*). This continuum of different migratory behaviors, which is very different from the stereotyped single-cell behavior found for isolated cells (11, 13, 14), suggests that there is a strong effect of the

Author contributions: S.V., S.T., H.B., and S.R.Q. designed research; S.V., S.T., and D.M.J. performed research; S.V., S.T., H.B., and S.R.Q. analyzed data; and S.V., S.T., H.B., and S.R.Q. wrote the paper.

The authors declare no conflict of interest.

This article is a PNAS Direct Submission.

Freely available online through the PNAS open access option.

Data deposition: A MATLAB implementation of the model presented in the paper has been deposited at SourceForge.net, http://sourceforge.net/projects/cell-migration/.

[1]S.V. and S.T. contributed equally to this work.

[2]To whom correspondence should be addressed. E-mail: quake@stanford.edu.

This article contains supporting information online at www.pnas.org/lookup/suppl/doi:10.1073/pnas.1204291110/-/DCSupplemental.

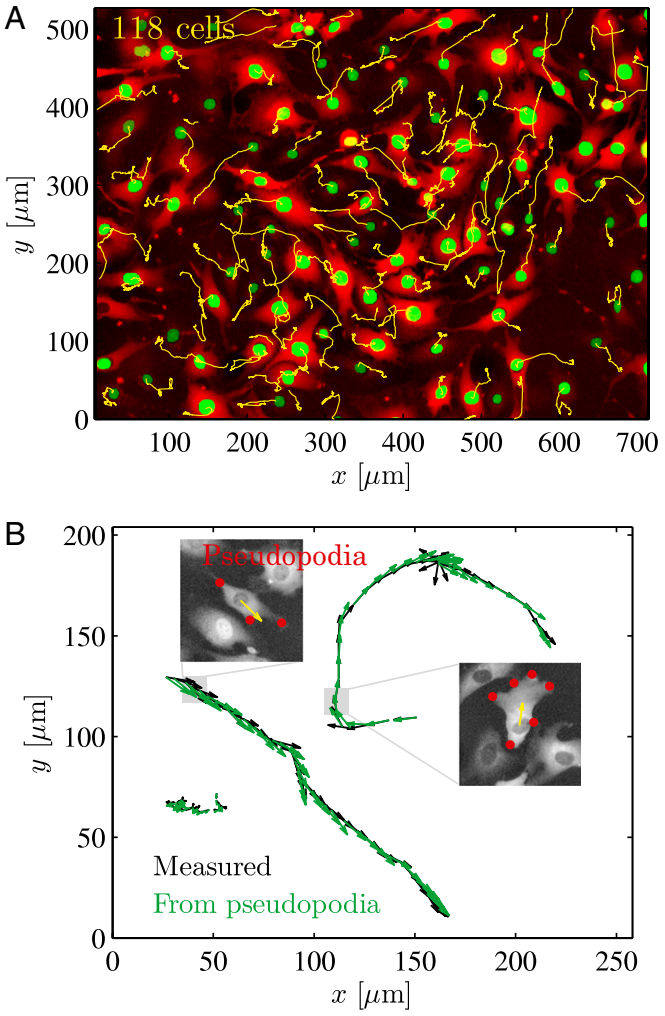

Fig. 1. Trajectories of the cells generated during the first 200 min of an experiment. (*A*) Trajectories (yellow) displayed on top of the fluorescence image illustrating the different fusion proteins used for the cytosols (red) and nuclei (green). (*B*) Trajectories can be nominally straight, curve, or display little apparent directionality. The vectorial sum of the pseudopodia of the cell (marked by red in insets) predicts the observed movement, because each pseudopod applies nominally the same force (20).

social context on the migration of the individual, even in the absence of cell–cell linkages (24–26). To fully understand this effect, including whether it is due to inherent cell–cell motility variations or is an emergent group property, we quantified all aspects of the migration using a number of cooperating statistical measures that together fully characterize the migration.

We first focus on an experiment at intermediate cell density ($\bar{d}_{\min} = 91.1$ μm) to introduce our statistical measures and illustrate our key findings. The speed of the individual cell fluctuates substantially as a function of time (Fig. 2*A* *Inset*) with similar single-cell speed distributions (Fig. 2*A*), and the average single-cell distribution from one experiment displays a distinct non-Gaussian tail (Fig. 2*B*) that has previously been shown to be a general feature of non-sheet-forming motile cells (37). The existence of similar non-Gaussian single-cell speed distributions suggests by the central limit theorem that each cell does not have an inherent velocity scale, but rather that cell speed is a dependent variable. The simultaneous observations of fluctuating single-cell speed and cell velocity being a dependent variable is consistent with pseudopodia-driven motility (*SI Appendix*).

To quantify the variations in total space sampled by the individuals we introduce the "maximum path distance" (MPD), defined as the maximum distance between any two points on the trajectory of the individual cell. This measure, which is equivalent to the span dimension of polymer physics (38), displayed large variations across the population, with large and small MPD values corresponding to cells moving nominally straight and cells that displace themselves small distances, respectively (MPD is nontrivially related to variations in single-cell trajectory curvature).

The observed variations in trajectories could be caused by a relative lack of collisions; however, we observed cells moving nominally straight even though they were in direct contact with other cells, as well as cells without direct contact with other cells displaying little long-term directionality (Movie S1). This indicates that collisions are not solely responsible for the variations in migratory behavior, and so to further investigate this single-cell directionality, we compute the directional autocorrelation of the cellular trajectories using the unit vectors in the direction of instantaneous velocity (*SI Appendix*, Eq. **S3** and Fig. 2*D*). This measure describes the average alignment of the direction of motion of the same cell over time and therefore measures the persistence of the direction of motion. Using the unit vectors in the direction of instantaneous velocity as opposed to the velocity vectors themselves removes any bias from the fluctuating speed and sets the range from 0 (no correlation) to 1 (complete correlation). The chamber-mean directional autocorrelation, which is representative of the majority of the cells (outliers only nominally affect the mean because the kurtosis is everywhere low; *SI Appendix*, Fig. S5), shows that the instantaneous step taken by each cell is positively correlated with the previous steps (Fig. 2*D*). The first sharp drop-off between the first and second time points occurs because changes in directionality are measured only every 4–6 min, and the rest of the data are well described by a decaying exponential $\phi e^{-\tau_{\text{lag}}/\tau_{\text{p}}}$. Here, the persistence time of directionality τ_{p} and the weight ϕ (varying from 0 to 1) describe, respectively, the time for the average cell to randomize its direction and the extent of directional motion in the chamber, with higher values of ϕ indicating a larger fraction of directionally persistent cells. For the present experiment we found $\phi = 0.46$ and $\tau_{\text{p}} = 69$ min.

Varying the cell density, we continue to observe straight-moving cells at all densities (Fig. 2*E*) even though each cell at intermediate and high densities experiences many collisions (and the ratio of cell surface area to total available chamber area is around 0.8 at all times; *SI Appendix*). The fraction of directionally persistent cells decreases at higher densities, but the persistence time of the individual cells remains essentially constant. This is illustrated by the decrease of the weight ϕ and the constancy of persistence time of directionality τ_{p} in Fig. 2 *F* and *G*. The average single-cell speed distribution is also independent of density, and this is well-fitted by generalized extreme value (GEV) distribution, which forms a natural parameterization (Fig. 2*H*; example fit shown in Fig. 2*B*). Both our measurements of speed distribution and the low-density limit of the directional autocorrelation agree with previous results for human fibroblasts (11) (the latter indicated by dashed lines in Fig. 2 *F*–*H*; compare with *SI Appendix*, Fig. S4). These findings indicate that the observed directionality does not depend on the fluctuating speed of the single cell, and the small variations in τ_{p} both within and across densities suggests that the directional persistence of motion, unlike cell speed and trajectory, is an inherent property of the cell's motility apparatus (i.e., internal polarization). Furthermore, the convergence of all our statistical measures to the level of isolated cells at $\bar{d}_{\min} \approx 120$ μm determines the critical density where the social context becomes important.

Pseudopod Formation and Lifetime Is Affected by Social Context. We verified that the cell migration in the social context is also mediated by pseudopodia (Fig. 1*B* and Movie S2), and so to probe the origin of the diverse cellular migratory behavior we therefore next

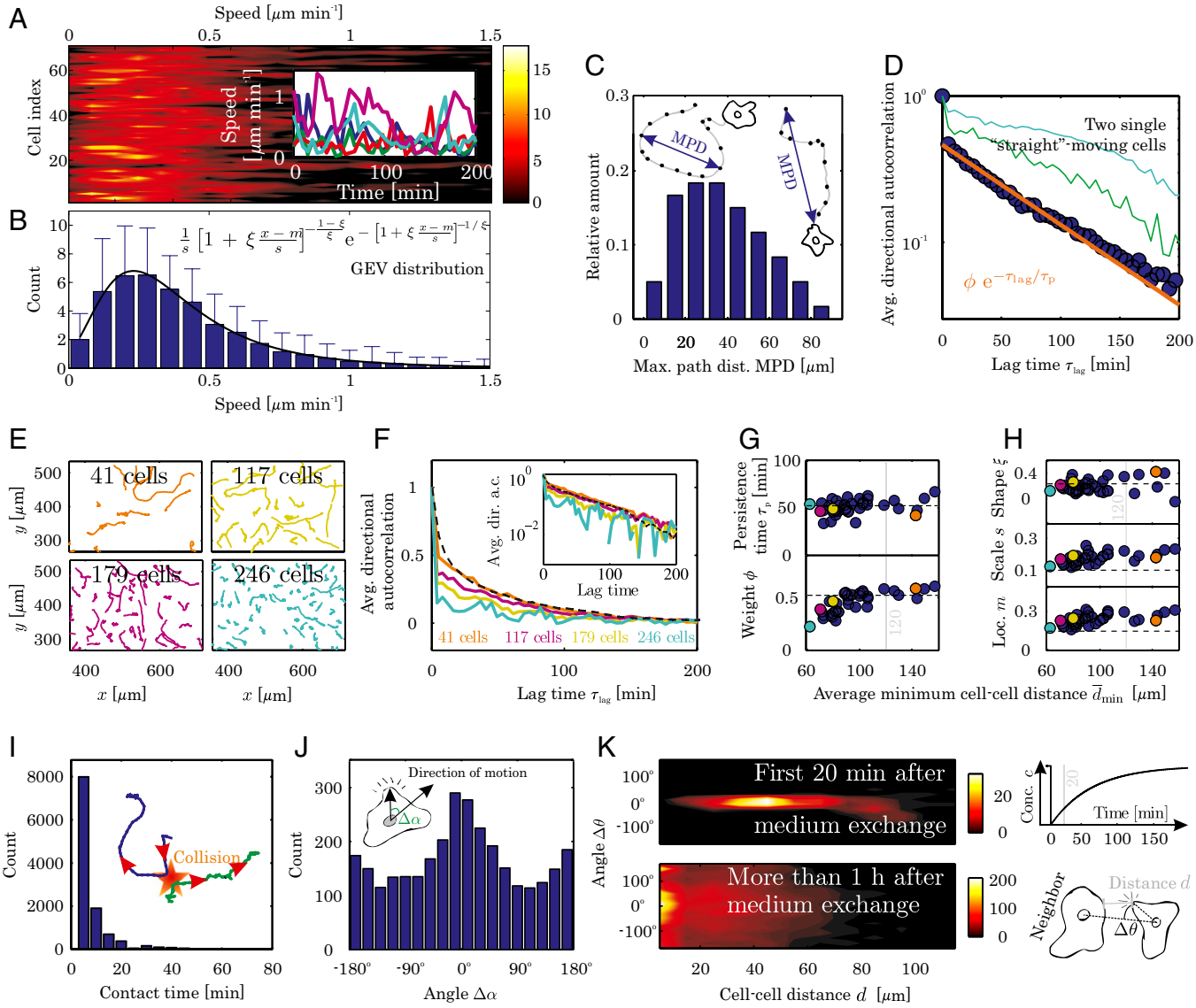

Fig. 2. Experimental observations of cell migration and pseudopodia. (*A*) Single-cell speed distribution, with inset showing speed vs. time for four single cells. (*B*) Average single-cell speed distribution (blue; error bars indicate SD) is well fitted by a generalized extreme value (GEV) distribution characterized by the location parameter *m*, the scale parameter *s*, and the shape parameter ξ. (*C*) Population distribution of single-cell maximum path distance (MPD). (*D*) Chamber-average directional autocorrelation (blue circles) and fit (orange line). Also shown are single-cell autocorrelations from two sample cells moving nominally straight (lines). The SD of the distribution decays from ±0.20 min close to $\tau_{lag} = 0$ to ± = 0.01 at $\tau_{lag} = 200$ min (*SI Appendix*, Fig. S5). (*E–H*) Effect of density on collective cellular migration; dashed lines in *F–H* indicate results for isolated cells extracted from ref. **11** (compare with *SI Appendix*, Fig. S4). (*E*) Examples of trajectories (compare with *SI Appendix*, Fig. S2) and (*F*) the corresponding average directional autocorrelations that follow the same exponential decay (*Inset*). (*G*) Weight ϕ and persistence time τ_p from least squares fits of average directional autocorrelations to $\phi\ e^{-\tau_{lag}/\tau_p}$ as a function of the average minimum nucleus-nucleus distance $\bar{d}_{min}$ in the chamber showing that persistence time τ_p is not affected by the changing density whereas the weight factor ϕ decreases due to higher collision rate. (*H*) Location *m*, scale *s*, and shape ξ from least squares fits of average single-cell speed distributions to the GEV distribution remains constant across densities. (*I*) Time periods of contact for colliding cell pairs (combined for all densities) is heavily dominated by short times, and the distribution is independent of cell density (*SI Appendix*, Fig. S8*A*). Also shown are the actual trajectories of two colliding cells (blue and green), with red arrows indicating direction of motion. (*J*) Pseudopod formation angle Δα with the current direction of motion (pooled across densities) shows a clear a clear preference of pseudopod formation in the current direction of motion, although pseudopodia are observed to form at all angles. This distribution is independent of cell density (*SI Appendix*, Fig. S8*C*). (*K*) Position and angle of pseudopod formation Δθ in relation to the nearest neighbor cell. At time $t = 0$, the entire volume of the microfluidic chamber is replaced with fresh media, effectively removing any chemokine background and allowing new chemokine gradients to be established (see schematic to the right). The cells overwhelmingly move to the nearest neighbor during the first 20 min after media replacement but only mildly so (and only when the nearest neighbor is very close) after 60 min, indicating that secreted chemokines induce pseudopod formation (*SI Appendix*).

investigated their pseudopodia. Colliding pseudopodia of different cells transiently remain in contact before they collapse (39) in a process known as contact inhibition of locomotion (2) (Movie S3), which is presumably achieved by locally depolymerizing the actin cytoskeleton with associated cessation of the local force. The distribution of contact times is strongly dominated by short times and exhibits no dependence of density (Fig. 2*I* and *SI Appendix*, Fig. S8*A*). We found a distribution of pseudopod lifetimes with a mean of 11.8 min (*SI Appendix*, Fig. S6*A*), so the directional persistence of ∼50 min indicated by the autocorrelation analysis (Fig. 2 *D* and *G*) can only be maintained by the cells through ordered pseudopod formation. Further investigations indicated that

pseudopod formation is dominated by independent biases by the current direction of motion (Fig. 2*J*) and chemicals (chemokine) secreted by the cells (Fig. 2*K* and *SI Appendix*, Table S2). Evidence of the former was found by computing the angle between the current cellular direction of motion and the position of pseudopod formation (Fig. 2*J*), which displayed a clear bias for the present direction of motion that is probably mediated by an internal polarization of key molecules (40), whereas evidence for the latter was found by studying the influence of neighbor cells in biasing pseudopod formation: Pseudopodia formed exclusively toward the nearest neighbor cell during the first 20 min after medium replacement (Fig. 2*K Upper*), but much less so when the analysis was redone starting 60 min after replacement (except when the neighbor is very close; Fig. 2*K Lower*). The effect was reproduced following additional media replacements in separate control experiments (*SI Appendix*, Fig. S9). Because these cells both posses chemotactic ability and furthermore are known to secrete some chemokines (*SI Appendix*), this effect is most likely caused by one or several secreted chemokine(s), as evidenced by the decrease of the response at later times except very close to neighbors and corroborated by the fact that most chemokine molecules have diffusivities on the order 10^{-10} $m^2 \cdot s^{-1}$, which sets the time scale for chamber filling to ~40 min. In other words, the secreted chemokines will have saturated the chamber by 40 min, effectively reducing chemokine gradient depths and the signal-to-noise ratio of chemokine receptor activity. Moreover, the constant base level of pseudopod formation observed in our investigation of directional bias (Fig. 2*J*) further illustrates the existence of an additional and independent pseudopod formation biasing system that on average is independent of the current direction of motion, and therefore is likely achieved by the chemokine bias. Although we did observe new pseudopods arising from splitting of existing pseudopodia, similar to the predominant origin of pseudopods observed in isolated cells (14), this was found to be secondary to the biased de novo formation of pseudopods just described (*SI Appendix*, Fig. S7). These observations indicate that the motile apparatus of the individual cell is centered around maintaining a certain direction through an internally controlled pseudopod formation bias (polarization), and that being in a social context introduces a second mechanism based on chemokine-mediated biasing, similar to findings in a previous report for *Dictyostelium* cells (41), as well as a higher frequency of pseudopod formation due to collisions.

Physical Model. To investigate whether these observed traffic rules on the individual cell level indeed do cause the very varied collective motion we observed, we formulated an agent-based mathematical model using the simplest physically reasonable assumptions for the motion of the individual cell based on three types of input: (*i*) our own pseudopod observations, (*ii*) previous experimental studies on chemotaxis of isolated cells, and (*iii*) Newton's second law of particle motion (*SI Appendix*, *Model Details*). This model, which can be considered an extension of the Vicsek model (21, 22, 42), exploits known cellular biophysics to simulate our experiments with a few hundred cells, a regime that is inaccessible to continuum modeling (43, 44). Model cells (Fig. 3*A*) dynamically form pseudopodia that each apply a force $\mathbf{F}_i$ of constant magnitude F_o radially away from the nucleus. In a time interval Δt the resultant force moves the cell a distance Δx, or equivalently imparts a velocity $\mathbf{v} = \Delta x/\Delta t$ given by

$$\gamma \mathbf{v} = \sum_i \mathbf{F}_i, \qquad [1]$$

where γ is a friction coefficient assumed to be identical for all model cells. Pseudopod formation is biased by the current direction of motion and a spatiotemporal field of chemokine concentration secreted by all cells. We use biased stochastic pseudopod activation because of the large thermal fluctuations in the low concentrations of intra- and extracellular chemicals. Touching pseudopodia of colliding cells collapse, and their local forces stop because of contact inhibition of locomotion. We furthermore assume chemokine secretion is identical for all cells; that force, collision times, and chemokine response function is the same for all pseudopodia; and that this function is a Hill function of the local relative chemokine concentration (Fig. 3*C*). All model parameters are determined either directly from the data (such as Fig. 2 *I* and *J*) or from reported literature results, except for the cell friction coefficient γ, of which no reliable measurements exist. We determined γ from the ensemble average of velocity distribution data by fitting one simulation to one experiment; having determined this single parameter the model predicts all statistical aspects of the collective motion. This is shown below through a number of statistical tests. Although simpler theoretical models have been presented in the past with the objective of investigating certain traits of the collective migration phenomena (21, 22, 37, 42–45), none of these models is able to simultaneously account for a wide variety of the migration data such as ours, and our model thus provides one of the simplest ways of incorporating all of our observations in a physically transparent formulation.

Comparison with Experiments. The model results are summarized in Fig. 3 and demonstrate quantitative agreement with the experiments in terms of single-cell speeds (Fig. 3 *D* and *E*), trajectories (Fig. 3 *B* and *G*), and directionality (Fig. 3*F*), thereby verifying our experimentally derived hypotheses of the role of the social interactions on motility (*SI Appendix*, Fig. S10 and Movie S4). The model quantitatively reproduces across cell densities—with a single value of γ—that the individual cells have the same nonnormal speed distribution (Fig. 3*D*) with an average that is similar to the experimental average (Fig. 3*E*); the exponentially decaying autocorrelation (Fig. 3*F*) including the changes in the weight factor ϕ, indicating the importance of the social interactions; and both the shape and range of the distribution of maximum path distances (Fig. 3*G*). The model also predicts the existence of cells moving along almost straight lines for the entire experiment (Fig. 3*B*) and the maximum path distance for these cells [largest single-cell measurements of maximum path distances are the same for model and experiment Fig. 3*G*)], but it does underpredict the ratio of these cells, as indicated by smaller tail of model predictions in Fig. 3*G*. In addition, the model value of $\gamma = 39$ $kg \cdot s^{-1}$ is in fair agreement with an estimate of $\gamma \approx 29$ $kg \cdot s^{-1}$ extracted from ref. 20 but is roughly one order of magnitude greater than an estimate from endothelial cells and a *Dictyostelium* slug (46) (*SI Appendix*). Although the model captures many features of our single-cell microscopy data, it falls short of perfectly reproducing the tail of the speed distribution (Fig. 3 *D* and *E* and *SI Appendix*, Fig. S11), likely because of the assumption of identical and time-independent pseudopod forces (*SI Appendix*). The model furthermore also does not precisely capture the exact shape of the average directional autocorrelations (Fig. 3*F*), indicating that directional persistence is likely achieved through a more complex machinery than is assumed in the model.

Discussion

The agreement of model predictions with experimental data for all of the emergent properties presented in Fig. 3 suggests that the subprocesses included in the model govern the motility. We therefore arrive at the following explanations for our observations: The dynamically changing positions of pseudopodia cause large fluctuations in speed at all densities, whereas directional persistence is achieved primarily by the directional bias of pseudopod formation but heavily influenced by both collisions and the secreted chemokine. The cells at low density are effectively isolated as they rarely collide and the nominally isotropic chemokine field

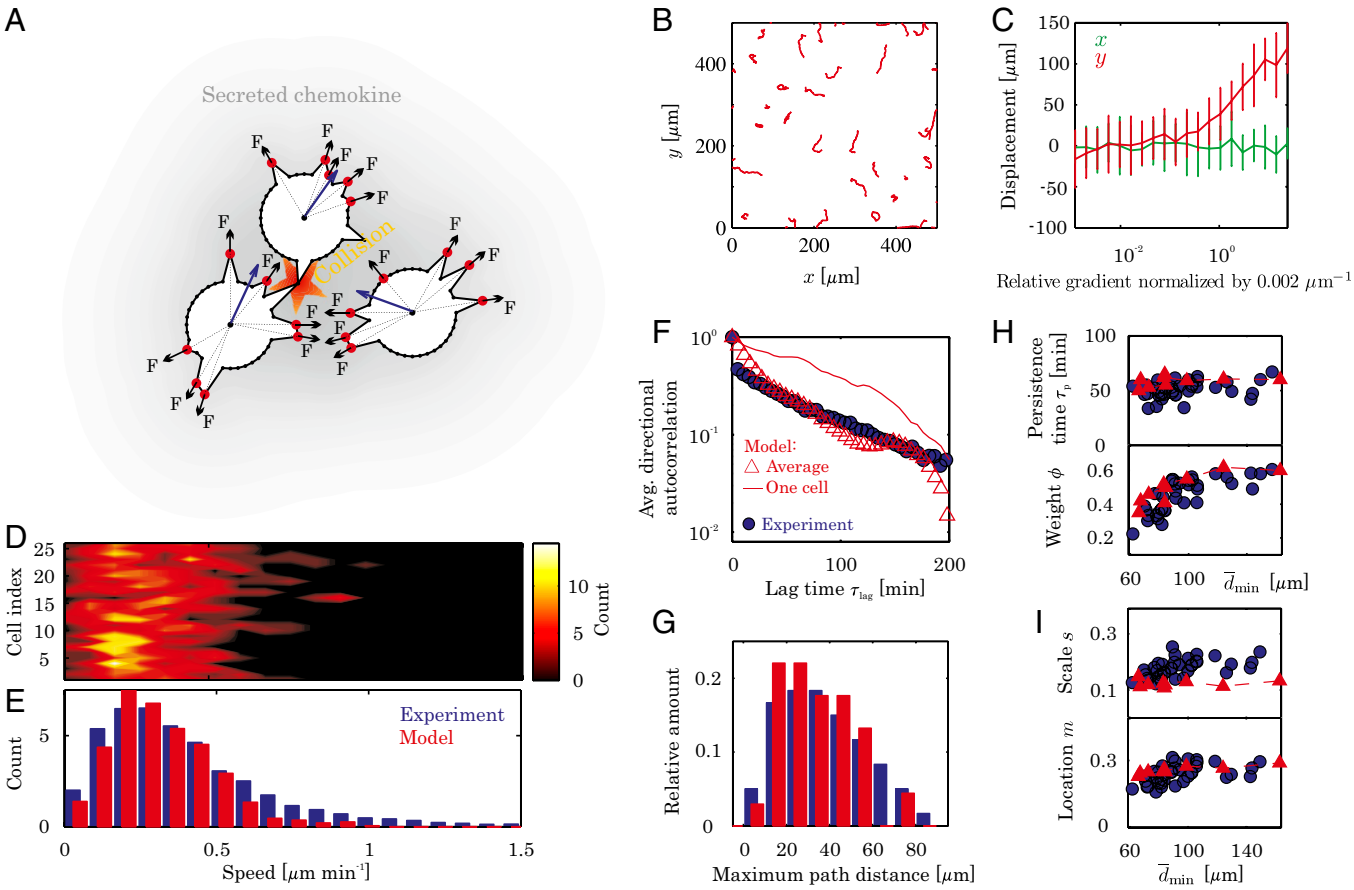

Fig. 3. Model formulation and predictions (model, red; experiments, blue). Experimental data are the same as in Fig. 2. (*A*) Single cells move by dynamically and stochastically forming pseudopodia (red) while they secrete chemokine, with each pseudopod providing a force, and colliding pseudopodia collapse. (*B*) Example model trajectories. (*C*) Average displacement in a 300-min simulation for different relative gradients (the gradient is applied only in the *y* direction) illustrate that model cells reliably respond to gradients above 0.002 μm·m^{-1}, as experimentally observed by Melvin et al. (16). The simulation was repeated 20 times for a single cell at each gradient level and error bars indicate SD. (*D*) Single-cell speed distributions (compare with Fig. 2*A*). (*E*) Average single-cell speed distribution, showing excellent agreement with experiments. (*F*) Chamber-averaged directional autocorrelation and one single-cell autocorrelation from a cell moving nominally straight (compare with Fig. 2*D*; compare with *SI Appendix*, Fig. S5. (*G*) Population distribution of maximum path distance (blue, experiment; red, model). (*H* and *I*) Model results across densities with the latter expressed by the average minimum cell-cell distance $\overline{d}_{\min}$ (red, model; blue, experiment). (*H*) Weight ϕ and persistence time τ_p for the fit to $\phi e^{-\tau_{lag}/\tau_p}$. (I) Location parameter *m* and scale parameter *s* in fit of average speed distribution to a GEV distribution. The shape parameter ξ (*SI Appendix*, Fig. S11), describing the tail of the distribution, is not well captured by the model because it underpredicts this part of the speed distribution, as seen in *E*.

therefore has little influence on the positions of new pseudopodia, whereas high collision rates at high densities lead to constant randomization of pseudopodia positions and low ϕ. At any density, straight-moving cells execute this motile behavior because their lateral pseudopodia are more often suppressed by lateral collisions with other cells or abruptly changing, large chemokine gradients. Cells displaying little overall directionality constantly have their direction of motion cut off, leading to many collisions, whereas curling cells experience few collisions and/or a clear and slowly moving chemokine bias. The observed continuum of different trajectories is therefore a direct consequence of the fluctuating near-cell environment and is no more surprising than similar observations of very varied trajectories of many interacting bodies obeying Newtonian mechanics. The model thus provides a comprehensible description of social cell migration that captures all of the complexity formulated in terms of biophysically well-defined single-cell quantities and, furthermore, illustrates how very complex biological behavior emerges from simple interaction rules.

Contrary to several other cell types, such as keratocytes (22), 3T3 fibroblast cells do not exhibit large-scale multicellular organization such as flocking (21). Fibroblasts deviate from these flocking cell types by not having strong local alignment of the neighbors, which therefore must be considered critical in achieving flocking. We nonetheless hypothesize that the observed effects of the neighboring cells on single-cell migration is highly relevant at physiological conditions. Within a population, the high collision rate continuously randomizes the directionality of the individual cells, so that on average there will always be cells moving away from the population. In the presence of an external signal, some of these boundary cells will be correctly aligned with this signal and will reliably move up the gradient, with the directional persistence providing the initial stabilization of the movement away from the population. This mechanism provides a directionally isotropic and fast sensor of external signals for the population, even though the single-cell polarizations vary and single-cell realignment with the external signal would occur on the time scale of directional persistence (τ_p). Whereas this social effect is fundamentally different from flocking and other social effects such as quorum sensing, it is another example of how nature achieves group-level dynamics of ignorant individuals for biological function beyond the control of the individuals by simply modulating the signal at the level of the individual through increased cell density. This mechanism could be a general biological principle underlying emerging population

behavior, yet the underpinnings, limits, and consequences remain to be investigated.

In summary, our investigations of social cell migration for thousands of cells at different densities have revealed a diverse migratory behavior that is largely controlled by the changing environment: Whereas the single cell tries to maintain its current direction of motion through preferentially forming pseudopodia in this direction, secreted chemokine-induced pseudopod formation along with collisions lead to pseudopod collapse, resulting in much more complex migratory behaviors than those reported for isolated cells, even in the absence of cell–cell variations. A simple model based on these observations quantitatively reproduces most migration behaviors across densities, including the existence of outliers, illustrating that these are the intercellular rules governing migration. In addition to their biological significance, our findings illustrate how complex biological behavior arises as a physical consequence of noisy single-cell behavior and interactions among the individuals, open a path for the derivation of continuum theory, and illustrate the importance of single-cell data in understanding such behavior.

Materials and Methods

Cell Line and Microfluidic Cell Culture Experiments. We used newly thawed $p65^{-/-}$ mouse fibroblast (3T3) cells expressing the cytosolic fluorescent fusion protein p65-DsRed under control of the endogenous mouse p65 promoter as well as the nuclear marker H2B-GFP driven by the human ubiquitin C promoter. Cells were seeded at densities from 4,000–40,000 cells cm^{-2} (~40—400 cells per chamber) into microfluidic chambers and the external conditions were set to standard culture conditions [5% (vol/vol) CO_2 and 37 °C external temperature] and maintained at this level. To conduct the experiments we replaced the chamber volume with fresh medium and sealed the chamber (the cells remained in the same media during the entire experiment; some cells were also exposed to TNF-α). The cells were imaged at a constant rate either every 4 or 6 min in both GFP and DsRed fluorescence channels during the entire experiment (5–6 h). Details are given in *SI Appendix, Materials and Methods*.

Automated Image Analysis. Automated image analysis algorithms used to obtain cell trajectories and pseudopod statistics are detailed in *SI Appendix, Materials and Methods*.

Model. Details of model development and implementation in MATLAB are given in *SI Appendix, Model Details*.

ACKNOWLEDGMENTS. The authors thank Tobias Meyer for a critical reading of the manuscript. S.V. thanks Tobias Meyer, Sean Collins, and Feng-Chiao Tsai for stimulating discussions. S.V. was supported by Grant 2106-08-0018 "ProCell," under the Programme Commission on Strategic Growth Technologies, the Danish Agency for Science, Technology and Innovation.

1. Orlic D, et al. (2001) Bone marrow cells regenerate infarcted myocardium. *Nature* 410(6829):701–705.
2. Abercrombie M, Heaysman JEM (1953) Observations on the social behaviour of cells in tissue culture. I. Speed of movement of chick heart fibroblasts in relation to their mutual contacts. *Exp Cell Res* 5(1):111–131.
3. Abercrombie M, Heaysman JE (1954) Observations on the social behaviour of cells in tissue culture. II. Monolayering of fibroblasts. *Exp Cell Res* 6(2):293–306.
4. Yates CA, et al. (2009) Inherent noise can facilitate coherence in collective swarm motion. *Proc Natl Acad Sci USA* 106(14):5464–5469.
5. Ballerini M, et al. (2008) Interaction ruling animal collective behavior depends on topological rather than metric distance: Evidence from a field study. *Proc Natl Acad Sci USA* 105(4):1232–1237.
6. Helbing D, Farkas IJ, Vicsek T (2000) Simulating dynamical features of escape panic. *Nature* 407(6803):487–490.
7. Martin P, Parkhurst SM (2004) Parallels between tissue repair and embryo morphogenesis. *Development* 131(13):3021–3034.
8. Lecaudey V, Gilmour D (2006) Organizing moving groups during morphogenesis. *Curr Opin Cell Biol* 18(1):102–107.
9. Alberts B, et al. (2007) *Molecular Biology of the Cell* (Garland Science, New York), 5th Ed.
10. Friedl P, Wolf K (2003) Tumour-cell invasion and migration: Diversity and escape mechanisms. *Nat Rev Cancer* 3(5):362–374.
11. Selmeczi D, Mosler S, Hagedorn PH, Larsen NB, Flyvbjerg H (2005) Cell motility as persistent random motion: Theories from experiments. *Biophys J* 89(2):912–931.
12. Li L, Cox EC, Flyvbjerg H (2011) 'Dicty dynamics': Dictyostelium motility as persistent random motion. *Phys Biol* 8(4):046006.
13. Arrieumerlou C, Meyer T (2005) A local coupling model and compass parameter for eukaryotic chemotaxis. *Dev Cell* 8(2):215–227.
14. Andrew N, Insall RH (2007) Chemotaxis in shallow gradients is mediated independently of PtdIns 3-kinase by biased choices between random protrusions. *Nat Cell Biol* 9(2):193–200.
15. Keren K, et al. (2008) Mechanism of shape determination in motile cells. *Nature* 453 (7194):475–480.
16. Melvin AT, Welf ES, Wang Y, Irvine DJ, Haugh JM (2011) In chemotaxing fibroblasts, both high-fidelity and weakly biased cell movements track the localization of PI3K signaling. *Biophys J* 100(8):1893–1901.
17. Lauffenburger DA, Horwitz AF (1996) Cell migration: A physically integrated molecular process. *Cell* 84(3):359–369.
18. DiMilla PA, Barbee K, Lauffenburger DA (1991) Mathematical model for the effects of adhesion and mechanics on cell migration speed. *Biophys J* 60(1):15–37.
19. Schreiber CH, Stewart M, Duke T (2010) Simulation of cell motility that reproduces the force-velocity relationship. *Proc Natl Acad Sci USA* 107(20):9141–9146.
20. Munevar S, Wang Y, Dembo M (2001) Traction force microscopy of migrating normal and H-ras transformed 3T3 fibroblasts. *Biophys J* 80(4):1744–1757.
21. Vicsek T, Czirók A, Ben-Jacob E, Cohen I, Shochet O (1995) Novel type of phase transition in a system of self-driven particles. *Phys Rev Lett* 75(6):1226–1229.
22. Szabó B, et al. (2006) Phase transition in the collective migration of tissue cells: experiment and model. *Phys Rev E Stat Nonlin Soft Matter Phys* 74(6 Pt 1):061908.
23. Gail MH, Boone CW (1970) The locomotion of mouse fibroblasts in tissue culture. *Biophys J* 10(10):980–993.
24. Angelini TE, et al. (2011) Glass-like dynamics of collective cell migration. *Proc Natl Acad Sci USA* 108(12):4714–4719.
25. Reffay M, et al. (2011) Orientation and polarity in collectively migrating cell structures: Statics and dynamics. *Biophys J* 100(11):2566–2575.
26. Vitorino P, Meyer T (2008) Modular control of endothelial sheet migration. *Genes Dev* 22(23):3268–3281.
27. Trepat X, et al. (2009) Physical forces during collective cell migration. *Nat Phys* 5: 426–430.
28. Angelini TE, Hannezo E, Trepat X, Fredberg JJ, Weitz DA (2010) Cell migration driven by cooperative substrate deformation patterns. *Phys Rev Lett* 104(16):168104.
29. Tambe DT, et al. (2011) Collective cell guidance by cooperative intercellular forces. *Nat Mater* 10(6):469–475.
30. Travis J (2011) Mysteries of the cell: Cell biology's open cases. *Science* 334(6059):1051.
31. Waters CM, Bassler BL (2005) Quorum sensing: Cell-to-cell communication in bacteria. *Annu Rev Cell Dev Biol* 21:319–346.
32. Nadell CD, Xavier JB, Levin SA, Foster KR (2008) The evolution of quorum sensing in bacterial biofilms. PLoS Comp. *Biol.* 6:e14.
33. Gregor T, Fujimoto K, Masaki N, Sawai S (2010) The onset of collective behavior in social amoebae. *Science* 328(5981):1021–1025.
34. Gómez-Sjöberg R, Leyrat AA, Pirone DM, Chen CS, Quake SR (2007) Versatile, fully automated, microfluidic cell culture system. *Anal Chem* 79(22):8557–8563.
35. Skotheim JM, Di Talia S, Siggia ED, Cross FR (2008) Positive feedback of G1 cyclins ensures coherent cell cycle entry. *Nature* 454(7202):291–296.
36. Tay S, et al. (2010) Single-cell NF-κB dynamics reveal digital activation and analogue information processing. *Nature* 466(7303):267–271.
37. Czirók A, Schlett K, Madarász E, Vicsek T (1998) Exponential distribution of locomotion activity in cell cultures. *Phys Rev Lett* 81:3038–3041.
38. Wang Y, Teraoka I, Hansen FY, Peters GH, Hassager O (2010) Mean span dimensions of ideal polymer chains containing branches and rings. *Macromolecules* 44:403–412.
39. Carmona-Fontaine C, et al. (2008) Contact inhibition of locomotion in vivo controls neural crest directional migration. *Nature* 456(7224):957–961.
40. King SJ, et al. (2011) β1 integrins regulate fibroblast chemotaxis through control of N-WASP stability. *EMBO J* 30(9):1705–1718.
41. Samadani A, Mettetal J, van Oudenaarden A (2006) Cellular asymmetry and individuality in directional sensing. *Proc Natl Acad Sci USA* 103(31):11549–11554.
42. Yamao M, Naoki H, Ishii S (2011) Multi-cellular logistics of collective cell migration. *PLoS ONE* 6(12):e27950.
43. Saintillan D, Shelley MJ (2008) Instabilities and pattern formation in active particle suspensions: kinetic theory and continuum simulations. *Phys Rev Lett* 100(17):178103.
44. Lambert G, Liao D, Austin RH (2010) Collective escape of chemotactic swimmers through microscopic ratchets. *Phys Rev Lett* 104(16):168102.
45. Graner F, Glazier JA (1992) Simulation of biological cell sorting using a two-dimensional extended Potts model. *Phys Rev Lett* 69(13):2013–2016.
46. Larripa K, Mogilner A (2006) Transport of a 1D viscoelastic actin-myosin strip of gel as a model of a crawling cell. *Physica A* 372(1):113–123.

Migration of cells in a social context
Supplementary Information Appendix

Søren Vedel[1], Savaş Tay[2], Darius M. Johnston[3], Henrik Bruus[1], and Stephen R. Quake[3]
[1]*Department of Micro- and Nanotechnology, Technical University of Denmark, DTU Nanotech building 345 B, DK-2800 Kongens Lyngby, Denmark*
[2]*Department of Biosystems Science and Engineering, Swiss Federal Institute of Technology, ETH Zürich, Mattenstrasse 26, Basel, Switzerland*
[3]*Departments of Applied Physics and Bioengineering, Stanford University and Howard Hughes Medical Institute, Stanford, California 94305, USA*

I. MATERIALS AND METHODS

A. Cell lines

We used $p65^{-/-}$ mouse fibroblast (3T3) cells expressing the cytosolic fluorescent fusion protein p65-DsRed under control of the endogenous mouse p65 promoter as well as the nuclear marker H2B-GFP driven by the human ubiquitin C promoter. Both markers were created using lentiviral systems [1]. After cloning, the cells were frozen and newly thawed cells were used for each experiment to prevent 3T3 cell re-transformation and to minimize heterogeneity. The motility statistics of these cells agree with single-cell statistics found in the literature, e.g. [2].

B. Microfluidic cell culture experiments

Cells were seeded at densities from 4,000−40,000 cells cm^{-2} ($\sim 40-400$ cells per chamber) into microfluidic chambers and were cultured for one day to reach 15-100% confluence before experiments. The external conditions were set to standard culture conditions (5% CO_2 and 37 °C external temperature) and maintained at this level. During cell growth, 33% of the chamber volume was replaced with fresh media (DMEM) every hour using the nanolitre microfluidic pump, which resulted in vigorous proliferation of 3T3 cells. We made sure that cells were healthy, motile and proliferating before experiments.

We varied the cell density by precisely controlling the cell counts in each chamber during automated seeding. The cell counts were recorded at every time point during experiments by taking pictures and counting the number of GFP positive nuclei. This produced a well-controlled cell density in the chambers during the entire experimental duration. In the analyses, we considered only a region away from the chamber walls to avoid edge effects, and the number of cells in this region varies between chambers of purportedly identical density. Nevertheless, the number of cells in each picture is counted using the nuclear GFP signal and thus the numbers are exact. Therefore, instead of binning the data based on expected seeding density, we instead report the density-dependence of the data based on the average minimum cell-cell distance of all cells in a chamber over the entire experiment, $\overline{d}_{\mathrm{min}}$.

The microfluidic culture chip [3] allows the replacement of the entire culture media in less than a second, which results in a step-like removal of all secreted signaling molecules. Once the media was flowed in, the chambers were sealed and were imaged at a constant rate Δt_{samp} either every 4 or 6 min in both GFP and DsRed fluorescence channels during the entire experiment (5-6 hours). The cells remained in the same media during the entire experiment. All cell densities were tested in parallel chambers, up to 24 different microfluidic chambers at a time.

Upon completing the trajectory analyses of the non-stimulated cells, we compared these results to cells of the same cell line exposed to the inflammatory signaling molecule tumor necrosis factor (TNF)-α. We observed no difference in motility characteristics between non-stimulated cells and cells exposed to TNFα in the range 0.005 ng mL^{-1} to 100 ng mL^{-1}, see Fig. S1 (no TNF indicated by blue, high TNF by orange) which plots both the speed distribution and fits of the average directional autocorrelation to the function $\phi \mathrm{e}^{-\tau_{\mathrm{lag}}/\tau_{\mathrm{p}}}$ that was also used in the main text. Since we furthermore did not observe any variation in pseudopod statistics between the two populations we included the cells exposed to TNFα in the analysis.

In total we analyzed the motility of 8566 cells at various densities in 79 different chambers using five different chips. Each density was repeated at least once (each experiment on different chips) and the majority repeated several times, see Table S1. Small variations in $\overline{d}_{\mathrm{min}}$ between otherwise identical chambers are due to the finite number of cells present in each chamber. We have presented the data according to the measured $\overline{d}_{\mathrm{min}}$ rather than binning, since the actual nearest-neighbor distance is important due to the induction of pseudopods by secreted chemokine.

TABLE S1: Microfluidic experiments

Chip	Max. $\overline{d}_{\mathrm{min}}$	Min. $\overline{d}_{\mathrm{min}}$	Avg. $\overline{d}_{\mathrm{min}}$	# of exp.
1	142.8 µm	82.0 µm	103.0 µm	16
2	89.7 µm	72.0 µm	80.5 µm	24
3	95.7 µm	76.0 µm	84.8 µm	15
4	143.9 µm	61.8 µm	87.3 µm	22
5	69.7 µm	57.8 µm	63.7 µm	2

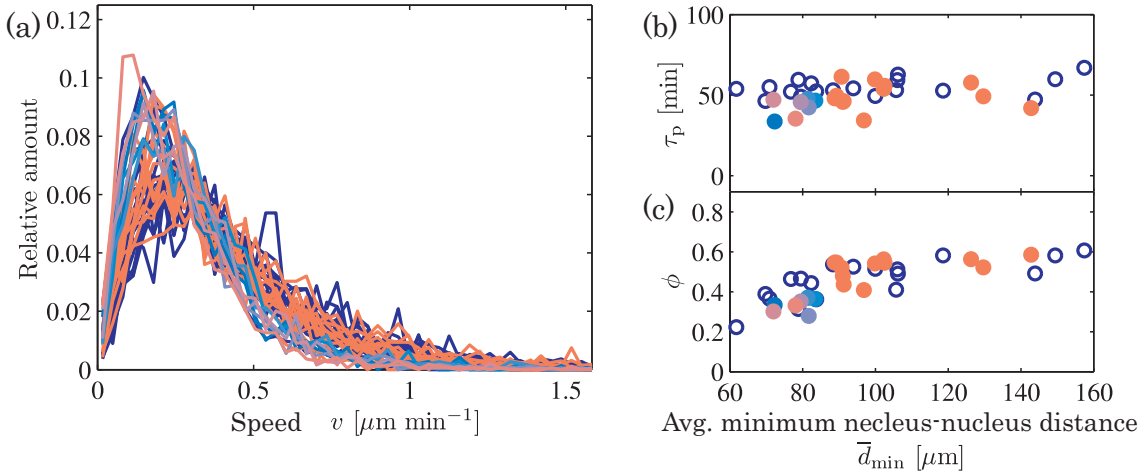

FIG. S1: Comparison between non-stimulated cells and cells exposed to the inflammatory signaling chemical TNFα shows no effect of the chemical. Each line in (a) and each circle in (b)-(c) is the average from one chamber. Non-stimulated cells are given by blue (open circles in (b)-(c)), results from stimulated cells are assigned a color ranging from light blue (lowest dose, 0.005 ng mL^{-1}) to orange (highest dose, 100 ng mL^{-1}) in ten steps (0.005, 0.01, 0.025 0.05, 0.1, 0.25, 0.5, 1, 10 and 100 ng mL^{-1}). (a) Chamber speed distribution. (b)-(c) Persistence time τ_p and weight factor ϕ (see Fig. 2 in the main text).

Good and unambiguous resolution of the cytosol boundaries are crucial for the correct detection of collisions and pseudopod dynamics (see below). We therefore compared the results of manual analysis of the pseudopodia of 10 non-stimulated cells to the results obtained from the automated analysis (see below) applied to the TNF-exposed data and found no variation. Given the agreement of the motility characteristics and the large range of TNFα investigated, we concluded that TNFα does not influence the motility.

C. Image analysis

To minimize human bias and errors we used automated algorithms to analyze the large experimental data set. Cells were imaged in both the GFP and DsRed channels with a Leica DMI6000B microscope (20× air objective) and Retiga-SRV CCD camera (Q Imaging) every 4-6 min for several hours. To generate the coordinates of single cells, custom MATLAB software using the Image Processing Toolbox was used to automatically identify the nuclei centroid from H2B-GFP images as previously described [4]. To identify nuclear regions, H2B-GFP images were local range contrast filtered with a neighborhood of three pixels and then thresholded, where the threshold level was automatically determined by k-means clustering pixel intensities with $k = 3$. Touching or merged nuclei (determined by solidity < 0.925) were then separated by a watershed transform with markers seeded at k-means clustered centroids. Nuclei were then linked to the nearest nuclei in the next time point and preliminary quality control checked for constant nuclear area through tracking. Cytoplasmic regions and p65-DsRed intensities were extracted through a combination of local thresholding and watershed transforms with the nuclei as marker seeds. All cell tracking was manually checked to eliminate mistakes by the automated analysis.

1. *Cell trajectories and velocities*

The centroid of the nucleus $\mathbf{x}^i(t_j) = (x^i, y^i)_{t_j}$ was used as the position of cell i at time $t_j = \Delta t_{\text{samp}}\, j$, $j = 0, 1, 2, \ldots$. Displacements $\Delta\mathbf{x}^i(t_j)$ and velocities $\mathbf{v}^i(t_j)$ were computed as

$$\Delta\mathbf{x}^i(t_j) = \mathbf{x}^i(t_{j+1}) - \mathbf{x}^i(t_j) \quad \text{and} \quad \mathbf{v}^i(t_j) = \frac{\Delta\mathbf{x}^i(t_j)}{\Delta t_{\text{samp}}}. \tag{S1}$$

The experimental noise in determining cellular position was estimated to ∼20 nm following the arguments in [5], with less than 0.2% of all recorded steps being below this limit (mean displacement between images was ∼25 times this limit). These small displacements were found dispersed between larger, admissible displacements for individual cells, with no correlation in time. Since the autocorrelation series of the cells that occasionally recorded displacements close to the level of positional noise did not show significant deviations from cells with only admissible displacements, taken from the same chambers, we concluded that all cell trajectories could be used without corrupting the conclusions.

2. *Collision and pseudopod analyses*

Cell outline coordinates were obtained from each image as the boundary of the cytosolic (p65-DsRed) region of each cell. Contact was defined as two pixels belonging

to separate cells being within 2 pixel from each other, and neighboring outline pixels in contact with the same cell were grouped into regions and linked in time using custom algorithms. For each region the times of contact $t_j,\ j, ..., j+N$ were stored, and the contact time was obtained as $t_{j+N} - t_{j-1}$. Only contacts starting after the first image and contacts ceasing prior to the last image in each series were used to ensure the entire lifetime of the contact was imaged.

Pseudopodia were detected from the cell outlines using a MATLAB implementation of the automated algorithm suggested by Bosgraaf and van Haastert [6], with small modifications. A pseudopod is an outward extension of the cell boundary, so following and edge-preserving smoothing step which removes pixelation noise, the algorithm determines the convexity of each node of each cell outline, with convexity ψ_n of node n defined by

$$\psi_n = \theta_n - 360/n - 180, \tag{S2}$$

where θ_n is the outer angle of the line segments pointing from the node to its two neighbors. $\psi_n > 0$ indicates convex (outward) and $\psi_n < 0$ indicates concave (inward) deflection from the outline. Regions of convexity (neighboring points with $\psi_n > 0$) were for each cell linked in time, and the tip of the region was at each time step identified as the center node.

A pseudopod was defined by at least 2 neighboring convex nodes, with the cumulative convexity of the neighboring nodes $\sum \psi_n$ exceeding 10° and the mean convexity gradient exceeding 4° μm^{-1}. Single concave nodes were allowed in a convex region, and one time step of slight concavity of a region was allowed if the same pseudopod existed both before and after the concave time point. While the algorithm was good at identifying pseudopodia, we found that it occasionally missed some, so each analyzed cell was manually checked to avoid bias introduced by the algorithm. Pseudopodia protrude and exert force for a period of time, before they collapse while providing little force. We computed the nucleus-tip distance between successive time steps, and included only growing (increasing distance) or stagnant (constant distance) pseudopodia in our analyses (Fig. 2 and Table I). Due to the sampling time of $\Delta t_{\rm samp} \approx 5$ min, some pseudopodia were present in only one image. Cell collisions locally cause the pseudopodia to retract, so we neglected all pseudopodia arising or dying at the times of collision. Furthermore, to avoid bias in the pseudopod life time analysis presented in Fig. S7(a), we first manually tracked pseudopod life times of ∼40 cells which did not collide and found no pseudopodia existing for more than 80 min. Next, using the automated analysis, we then obtained pseudopod life times from 154 cells which each went at least 80 min without colliding: within the collision-free interval we measured the life times of all pseudopodia starting at each time step. Finally, angles of pseudopod formation $\Delta\alpha$ in relation to direction of motion (Fig. 2(j) and Fig. S7(b)) were computed between the current vectorial displacement $\Delta \mathbf{x}^i(t_j)$ (see Eq. (S1)) and the vector connecting the nucleus tip and the pseudopod tip.

D. Directional autocorrelation analysis

The vectorial directional autocorrelation of all cells is computed using the unit vectors in the instantaneous direction of motion. For cell i at the lag $\tau_{\rm lag}$ this directional autocorrelation is given by

$$C_i(\tau_{\rm lag}) = \langle \mathbf{e}^i_j \cdot \mathbf{e}^i_{j+n} \rangle, \tag{S3}$$

where $\mathbf{e}^i_j$ and $\mathbf{e}^i_{j+n}$ are the unit vectors in the direction of motion of cell i (e.g. $\mathbf{e}^i_j = \mathbf{v}^i(t_j)/|\mathbf{v}^i(t_j)|$) at times $j\Delta t_{\rm samp}$ and $(j+n)\Delta t_{\rm samp}$, $\tau_{\rm lag}$ is related to the sampling time $\Delta t_{\rm samp}$ by $\tau_{\rm lag} = n\Delta t_{\rm samp}$, and the brackets denote average over all times. Since we do not have infinite time series, the results in Figs. 2 and 3 in the main text has been obtained from an unbiased estimate, similar to the one used in [5].

II. SUPPLEMENTARY DATA

We present here additional data to supplement the findings presented in the paper. Table S2 lists all observations and model predictions.

A. Density dependence, isotropic cell movement and convergence to isolated-cell migratory behavior

Figure S2 presents trajectories for four chambers supplementing the one set shown in the main text (Fig. 1(a)). Excerpts of these figures are shown in Fig. 2(e) in the main text. Figure S3 shows that there is no preferred direction of motion of the cells in a chamber, so the direction taken by each cell is random, although the motion of each cell depends on previous times according to Fig. 2(d), (f) and (g) in the main text. Figure S4 presents the speed distribution of isolated human fibroblasts from Selmeczi *et al.* [2] (dashed red line), which has been fitted to the generalized extreme value distribution to obtain the reference values presented as dashed black lines in Fig. 2(h) in the main text; the blue bars in the same figure shows our measurement.

B. Non-Gaussian speed distributions and pseudopodia-driven locomotion

The central limit theorem states that data from a large number of independent and identically distributed random variables will be distributed according to the normal distribution. If the random variables are not independent and/or identically distributed, the result is not a Gaussian distribution. Thus, if we were to assume that each

TABLE S2: Summary of all experimental observations and model predictions.

	Experimental observations	
Pseudopodia	Cells dynamically form these protrusions which apply traction force to the substrate	Fig. 1(b)
Pseudopod life times	Distributed with a mean of 11.8 min.	Fig. S6(a)
Pseudopod life time and direction of motion	Same life time distributions found whether pseudopodia form along or against the current direction of motion	Fig. S6(b)
Single-cell number of pseudopodia	Nominally constant over time for the individual cell, but variations among the cells	Fig. S6(c) and (d)
Directional pseudopod bias	Pseudopodia formation is biased in the current direction of motion	Fig. 2(j)
Local pseudopod formation bias by other pseudopodia through pseudopod splitting	No evidence that this is dominating although we do observe it	Fig. S7
Chemokine bias	Neighbor cells induce pseudopod formation by secreting a pseudopod-inducing chemical (chemokine)	Fig. 2(k)
Preferred direction of motion	No preferred direction of motion of the cells in a chamber	Fig. S3
Cell-cell collisions	Colliding cells transiently adhere to each other before the touching pseudopodia collapse, in a process known as contact inhibition of locomotion.	Fig. 2(i)
Single-cell speed	Fluctuating, but with similar distributions among cells indicating that all cells move. The average distribution is well fitted by a GEV distribution. Very similar across densities	Fig. 2(a),(b) and (h)
Single-cell trajectories	Some are almost straight, other curl, yet other exhibit little apparent directionality. Fraction of cells moving nominally straight decays at higher density	Figs. 1 and 2(c) and (e)
Single-cell directionality	Chamber-average directional autocorrelation (which well represents the individual) decays exponentially ($\phi e^{-\tau_{\rm lag}/\tau_{\rm p}}$) on a time scale of $\tau_{\rm p} = 50 \pm 11$ min. The weight factor ϕ decays at higher densities since a smaller fraction of cells move nominally straight	Fig. 2(d), (f) and (g), and Fig. S5
Cells moving nominally straight during whole experiment	Present at all densities	Fig. 2(e) and Fig. S2
	Model predictions	
Single-cell speed	Fluctuating with similar distributions among cells and all cells moving. Average model speed distribution quantitatively reproduces experiment	Fig. 3(d) and (e)
Single-cell trajectories	Some are almost straight, other curl, yet other exhibit little apparent directionality. MPD distribution is in quantitative agreement with experiment, but fraction of cells moving nominally straight is lower	Figs. 3(b) and (g)
Single-cell directionality	Chamber-average well represents the individual, and this average agrees with experiment	Fig. 3(f) and Fig. S5
Effect of density	Model quantitatively captures the experimental findings across densities	Fig. 3(h) and (i)

cell had a certain inherent velocity scale, we would expect that a large number of isogenic cells would present a Gaussian speed distribution. However, it is well-known that our cells move by pseudopodia so cell speed is a not independent variable, which is therefore not normally distributed since the conditions of the central limit theorem are violated. Hence, the existence of the non-Gaussian speed distribution illustrates that speed is not an independent variable.

Instead, our observation of fluctuating speed and similar single-cell speed distributions are consistent with cell speed being the result of pseudopodia-driven locomotion with transient pseudopodia: Each time a new pseudopod forms, the cell speed is changed, causing the observed fluctuations (Fig. 1(a) inset), while the fact that pseudopodia "drive" the cell means that cell speed is a dependent variable. The fact that similar average speeds are found among the cells is the result of the relative isotropic near-cell environment experienced on average, and the fact that each cell only produces a limited number of pseudopodia (likely due to limited amounts of the intracellular cytoskeletal components needed to form the pseudopodia; Fig. S6(c)). This argument follows a similar argument regarding non-Gaussian traction force distributions in sheets of mechanically interlinked Madin-Darby canine kidney epithelial cells [7].

C. Influence of outliers in chamber-averaged directional autocorrelation functions

The directional autocorrelation series of the individual cells in a chamber are not completely identical and consequently exhibit some variation, as shown by the non-negligible standard deviation of the distribution of directional autocorrelations (Fig. S5(a)). The data is for the experiment of Fig. 2(a)-(d) in the main text. Variations are expected for any biological system, but the decisive question is whether the outliers of the distribution significantly affect the mean, i.e. whether the population mean well represents the individual cell.

To investigate whether the chamber-average directional autocorrelation well represents the individual C_i we computed the kurtosis $\kappa(C_i)$ of the distribution of C_i at each lag time. The kurtosis measures the influence of the outliers in defining the mean, and the kurtosis of the normal distribution is 3. We find that the kurtosis of the distribution of single-cell directional autocorrelations is well described by the mean, since it is everywhere close to 3, see lower panel in Fig. S5(b) where the dashed line indicates $\kappa = 3$, the kurtosis of normal distribution.

D. Relevance of "straight" trajectories: coverage fraction of cell area to total chamber area

The straight trajectories found at all densities (see Fig. 2(e), (f) and (h) as well as Fig. S2) are not just a mere coincidence, but represent features of the dynamics of the cells' migratory behavior. To support this, we compute the coverage fraction of total cell surface area to total chamber area.

The total area of investigation in a cell culture chamber is

$$A_\mathrm{t} = 500\ \mu\mathrm{m} \times 700\ \mu\mathrm{m} = 3.5 \times 10^{-7}\ \mathrm{m}^2, \tag{S4}$$

while the projected surface area of one cell ($\sim$20 μm radius) is

$$A_\mathrm{c} = \pi \times (20\ \mu\mathrm{m})^2 = 1.2 \times 10^{-9}\ \mathrm{m}^2. \tag{S5}$$

We define the coverage fraction F_N of N cells as

$$F_N = \frac{N\,A_\mathrm{c}}{A_\mathrm{t}}, \tag{S6}$$

so since we have between 36 and 246 cells in the chambers, the coverage fraction varies from 0.12 (36 cells) to 0.84 (246 cells), while $F_N = 0.67$ is found for 100 cells. The fraction of available space for the cells to move on is at any instant $1 - F_N$. Since all the cells move, and we observe them over prolonged periods of time, it is very unlikely by pure chance to find the straight paths as simply just a consequence of a relative lack of collisions. Furthermore, one finds several cells in Supplementary Movie 1 moving along nominally straight lines even though they collide with other cells (even for some head-on collisions). The existence of straight trajectories at all densities emphasize that these trajectories do not arise out of pure chance, but indeed reflect features of the cell-cell interaction dynamics.

E. Supplementary pseudopod statistics

1. *Pseudopod life times*

Pseudopod life times are distributed with a mean of $\langle \tau_\mathrm{pseud} \rangle = 11.8$ min (Fig. S6(a)), and we find no dependence on pseudopod life time on whether they form along or against the current direction of motion (Fig. S6(b)), expressed by the angle $\Delta\alpha$ between the position of pseudopod formation and the current direction of motion (see also the schematic in Fig. 2(j)).

2. *Single-cell number of pseudopodia*

For the single cell, the number of pseudopodia as a function of time (ν) exhibits only small variations about a certain number (Fig. S6(c) inset), presumably due to a limited amount of intracellular actin. For each cell we take the mode number ν_m over time as the representative single-cell number of pseudopodia, and the distribution of these mode numbers varies between 1 and 7 (Fig. S6(c)). To quantify the variations about these mode numbers we define the standard variation about the mode number,

$$\sigma = \sqrt{\frac{1}{n-1}\sum_{i=1}^{n}(\nu_i - \nu_\mathrm{m})^2}. \tag{S7}$$

This measure is similar to the standard deviation, but while the latter is computed with reference to the mean, our measure is computed with reference to the mode number. We show in Fig. S6(d) that for all cells the standard variation about the cell-specific mode number is small, with a mean variation of $\langle \sigma \rangle = 1.35$ for the 154 cells presented in the figure.

3. *No local pseudopod formation bias by existing pseudopodia*

We did not find any dominating dependence of the position of pseudopod formation on the presence of existing pseudopodia, as reported for isolated cells [8]. To arrive at this result, we computed the angle $\Delta\beta$ between the position of formation and the nearest neighboring pseudopod. For completely random pseudopod formation, we expect a pseudopod to be present on average every $360°/\nu$ where ν is the current number of pseudopodia of the cell, while a strong induction of existing pseudopodia

on forming pseudopodia would lead to an angular difference independent of the number of existing pseudopodia. Grouping the results based on ν, see Fig. S7, we find the most occurring positions of pseudopod formation coinciding with the angular distance $\pm 360°/(2\,\nu)$ (indicated by the dashed lines in the figure), indicating that no dominating relationship exists between the positions of established pseudopodia and the positions of formation for new pseudopodia. This emphasizes the differences between being isolated and being in a social context. Since we do find significant positive correlation between pseudopod formation and both current direction of motion and secreted chemokines, we expect the variations are due to these effects and the limits set by finite statistics.

4. Pseudopod statistics are independent of cell density

The variations across cell densities (mean±s.d.) of pseudopod contact times during collisions (Fig. S8(a)), pseudopod life times (Fig. S8(b)) and pseudopod formation relative to the current direction of motion (Fig. S8(c)) suggests that these statistics are independent of cell density. In all three cases, the normalized pooled data across cell densities agrees with the averages taken over these densities, and the standard deviation is low. We therefore conclude that these statistics are independent of cell density.

F. Supporting information for the hypothesis of chemokine bias of pseudopod formation

We present here three independent lines of supporting information for the hypothesis based on Fig. 2(k) that one or more secreted chemokines induce pseudopod formation.

First, there is a large body of previous work documenting the chemotactic ability of fibroblasts to several chemokines, e.g. [9–13], and another large body of previous work establishing that the same cells secrete various chemokines e.g. [14–17], which together support the notion that these cells could secrete a chemoattractant. Taken together with the previous observations that higher local levels of chemoattractant favor pseudopod formation [9], this suggests that cell-secreted chemoattractants induce pseudopod formation.

Second, assuming that secreted chemokines do not contribute to pseudopod formation, in spite of this vast body of literature, the most obvious other candidates for the observations of preferred pseudopod-formation towards the nearest neighbor cell presented in Fig. 2(k) in the main text are [18]

(i) mechanical tension in the substrate applied by the cells (mechanotaxis), or

(ii) the attachment of pseudopod-inducing molecules to the substrate by either the cells themselves or as a result of the microfabrication procedures (haptotaxis).

The cells are incubated in the chamber for one day prior to media exchange and image acquisition, so the stress field in the substrate, which is sensed by cells in mechanotaxis, would not be expected to vary around flushing; our results in Fig. 2(k) therefore refute (i) as a possible explanation. Regarding (ii), if this was achieved by cells attaching pseudopod-inducing molecules to the substrate, this alternative would imply that cells either preferentially follow each other, or that pseudopods more often form where another cell previously was. This is contrary to our observations. If it was achieved by signaling molecules trapped during the fabrication procedure, we would expect that cells either move along certain paths in the chamber, or that they form pseudopods in specific directions when they are in specific positions in the chamber. These options are also both contrary to our observations. Finally, we would not expect any temporal dependence of a haptotactic response around flushing, which is of course contrary to our findings of Fig. 2(k). Thus, we can safely disregard haptotaxis and mechanotaxis as significant inducers of pseudopodia.

Third, we investigated the positions of pseudopod formation relative to the nearest neighbor cell for two independent experiments with complete media replacement every 2 h. Focusing only on the first 20 min following the first and second media replacement, we redid the analysis presented in Fig. 2(k). If our chemokine hypothesis is true, we would expect new pseudopodia forming in any 20 min segment following any media replacement to have small angle differences ($\Delta\theta \approx 0$) irrespectable of whether this was the first or second replacement. We show in Fig. S9 that this is indeed the case for the two independent experiments (see also explanatory schematic in Fig. 2(k)), with each column in the figure corresponding to a different experiment.

Taken together, these previously reported observations and our own experimental findings strongly suggest that a cell-secreted chemokine induce the formation of pseudopodia in the cells.

G. Examples of model-predicted chemokine fields

Chemokine concentration field predicted by the model are given in Fig. S10, with panel (a) showing the chemokine concentration field for a low-density simulation and Fig. S10(b) taken from the same numerical experiment as shown in Fig. 3(b) and (d)-(g) in the main text.

H. Interpreting γ

The cell friction coefficient γ is related to the energy dissipated by the making and breaking of cell-substrate

chemical bonds as the cell moves. Contrary to measurements of the strength of these bonds, the friction is rarely determined experimentally, and the irregularity, softness and general ignorance of the significant molecular contributors of the cell attachment during migration makes first-principles theoretical analysis difficult. A value of $\gamma \approx 29$ kg s^{-1} can be deduced from Munevar *et al.* [19] by estimating the forward traction force from a traction force map and using the stated average velocity. Similarly, and an order-of-magnitude estimate of the friction per unit cell surface area of 10^9 kg s^{-1} m^{-2} by Larripa and Mogilner [20] yields $\gamma \approx 1$ kg s^{-1} for a cell of radius 20 μm. This is an order of magnitude lower than our value of $\gamma = 39$ kg s^{-1}, but it should be borne in mind that the value in [20] was estimated from the reported work of others on endothelial cells and a *Dictyostelium* slug.

However, these numbers are many orders of magnitude greater than the viscous Stokes friction with the medium

$$\gamma_{\text{Stokes}} = 6\pi\eta r \tag{S8}$$

of $\gamma_{\text{Stokes}} \approx 4 \times 10^{-7}$ kg s^{-1}, where $\eta = 1.002 \times 10^{-3}$ Pa s is the viscosity of the liquid (assumed to be water) and $r \approx 20$ μm is the cell radius (Table S4). This is not surprising since the molecular interactions with liquid molecules is weaker than the interactions with attaching polymers used by the cells.

I. The tail of the speed distribution

Model speed distributions are fitted to the generalized extreme value (GEV) distribution in Fig. 3 of the main text, and Fig. S11 gives the fitted shape parameter ξ across densities. The shape parameter indicates the significance of the tail in the GEV fit of the speed distribution, and Fig. S11 shows that the model underpredicts the value of ξ. Physically, this implies that the model does not well capture the short burst of very high speeds produced with low probability by the cells. The overall agreement of the rest of the statistical measures for both speed, directionality and total sampled space, suggests that the model is nonetheless very capable of describing the overall dynamics, and since furthermore the model uses the experimental pseudopod statistics as input, a misrepresentation of these statistics can also be disregarded the source of the tail. Together, this suggests that the disagreement is likely due to the model assumption of constant force over time of identical magnitude F_{o} applied by each pseudopod, which indeed is a very naive picture of the dynamics of the molecular interactions causing the locomotion. Our model therefore indicates that speed time-dependent and perhaps graded pseudopod forces are found in real cells, but that these subtleties only have nominal influence on the overall dynamics.

J. Movies

Movie 1 The movement of cells at medium density in a chamber during 200 min. The trajectories are given by the yellow lines.

Movie 2 The positions and life times of the pseudopodia change dynamically during the course of an experiment, as illustrated for two cells. Pseudopodia are marked by red circles, with arrows indicating the actual direction of motion (green) and the direction of movement predicted from the pseudopodia (red).

Movie 3 The cells exhibit contact inhibition of locomotion. Colliding cells (marked by green) transiently remain in contact (for roughly 5.5 min, see Fig. 2(i)), before they move away from each other, followed by collapse of the touching pseudopodia of different cells.

Movie 4 Illustration of model cell migration behavior. Active membrane points are indicated by red dots, and the trajectories of the cells are indicated by the blue lines.

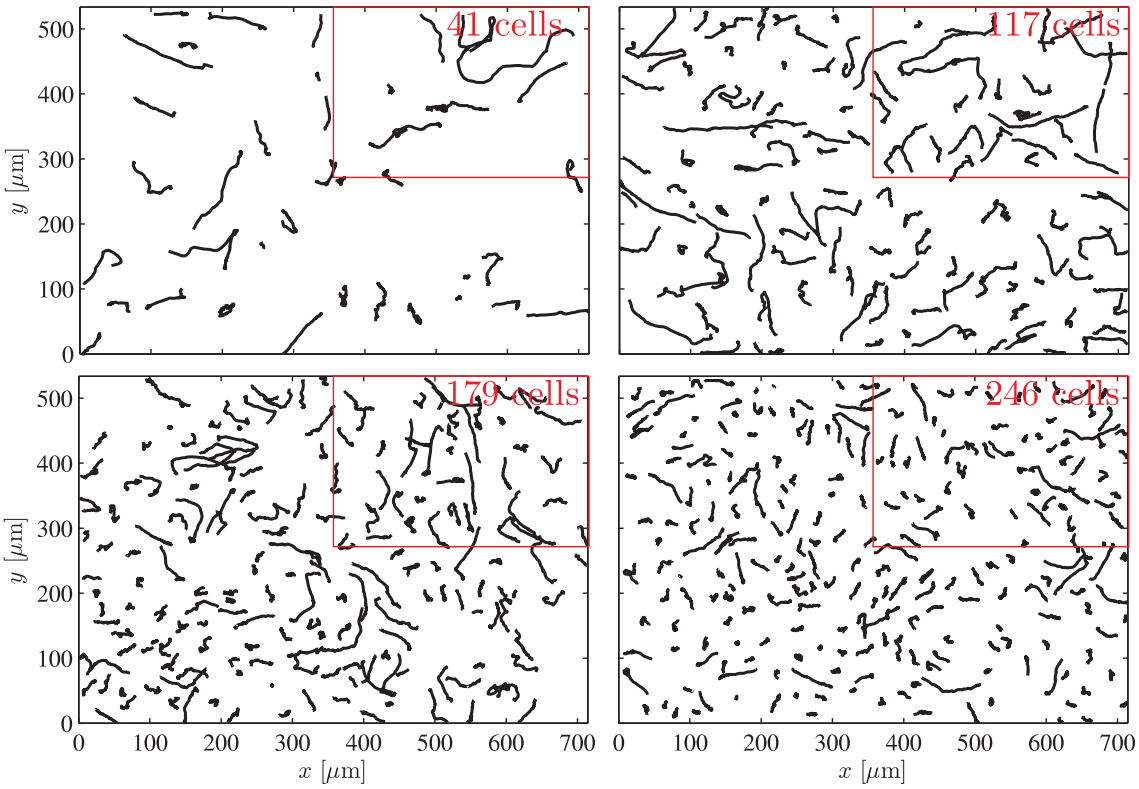

FIG. S2: Whole-chamber cell trajectories at four different densities. Exerts are given in Fig. 2(e) in the main text, with the exerts corresponding to the regions marked by red boxes. The average cell diameter is 41.7 μm (supplementary Fig. S12(a)), and the average minimum cell-cell distance varies from 149 μm at the lowest density to 45 μm at the highest.

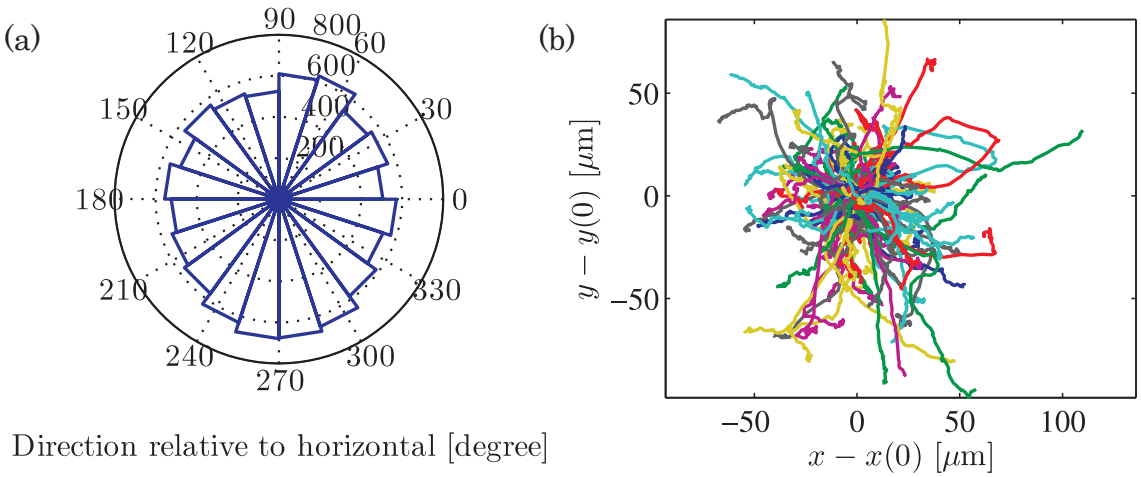

FIG. S3: The cell direction of motion is random, here illustrated by two different means for a single chamber. (a) Histogram of the instantaneous angle of motion relative to horizontal and (b) all trajectories shifted to the same starting position (initial position $\mathbf{x}(t = 0)$ has been subtracted, each trajectory is randomly given one of ten different colors) both confirm the absence of a preferred average direction of motion, within the limits of finite statistics.

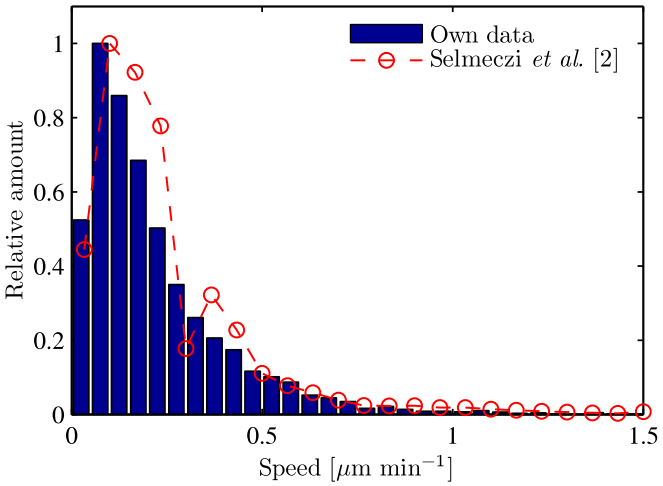

FIG. S4: Comparison of own speed distribution (blue bars) and the speed distribution of isolated human fibroblasts extracted from Selmeczi *et al.* [2]. The two distributions are in agreement.

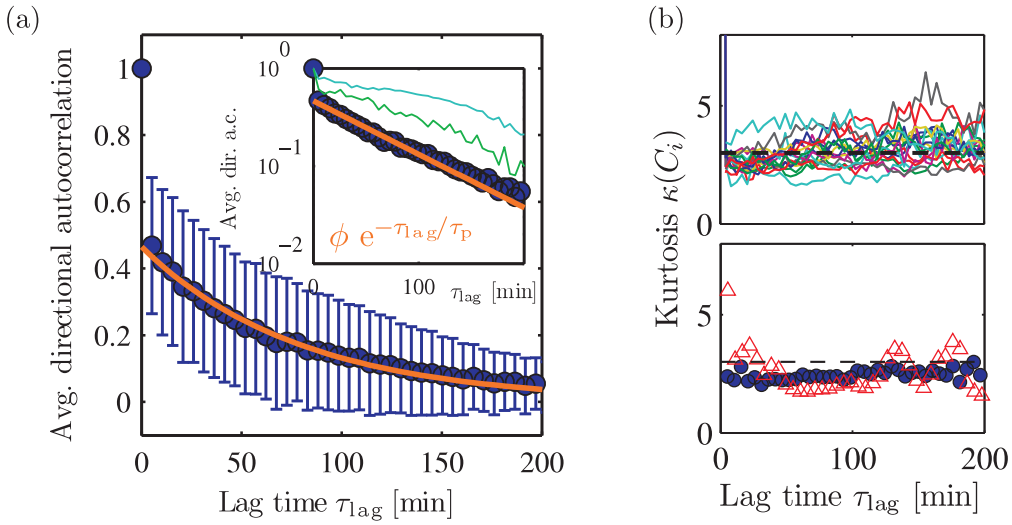

FIG. S5: Distribution of single-cell directional autocorrelations in an experiment. (a) Standard deviation of the distribution of single-cell directional autocorrelation functions shows some variation between the individual cells. The figure shows the result for a representative experiment (same as in Fig. 2(a)-(d) in the main text, lin-log version given in the inset) where the standard deviation decays from ± 0.20 close to $\tau_{\mathrm{lag}} = 0$ min to $\pm = 0.01$ at $\tau_{\mathrm{lag}} = 200$ min. (b) Kurtosis of the distribution of single-cell directional autocorrelation functions. Top panel illustrate individual experimental chambers, while the bottom panel illustrates the distribution for both model and experiment for the chamber presented in Figs. 2 and 3 in the main text. Dashed black lines indicate 3, the kurtosis of the normal distribution.

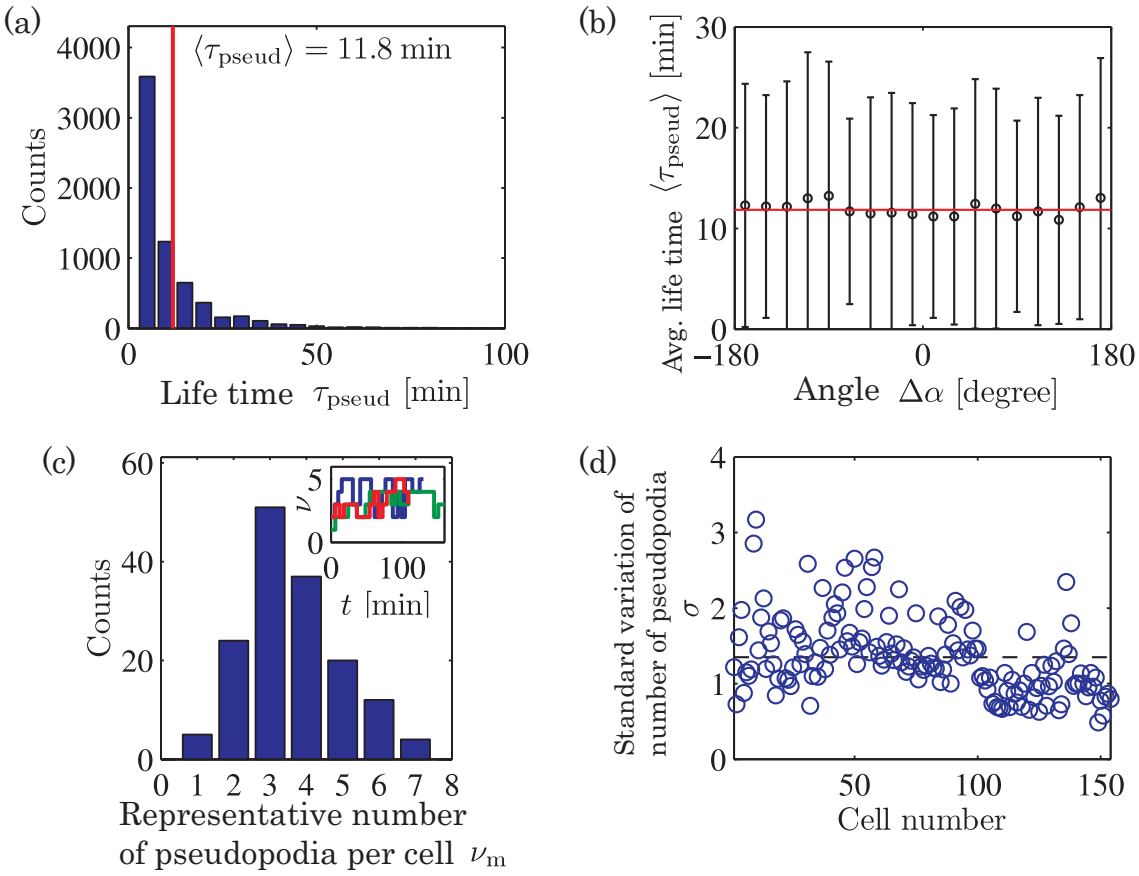

FIG. S6: Supplementary pseudopod statistics. (a) Pseudopod life times with red line indicating mean. (b) Pseudopod life times as function of the angle between the position of pseudopod formation and the current direction of motion. Red line indicates the mean life time for all pseudopodia (it is the same red line as in (a)). (c) Number of pseudopodia per cell is roughly conserved over time. Inset shows single-cell number of pseudopodia versus time and main panel gives the distribution of single-cell mode numbers over time of pseudopodia. (d) The standard variation σ, see Eq. (S7), of the instantaneous number of pseudopodia about the mode number of pseudopodia $\nu_{\rm m}$, computed for each cell, shows that the mode number is a representative measure of the cell's number of pseudopodia. The dashed black line gives the average for all cells in the figure, $\langle\sigma\rangle = 1.35$.

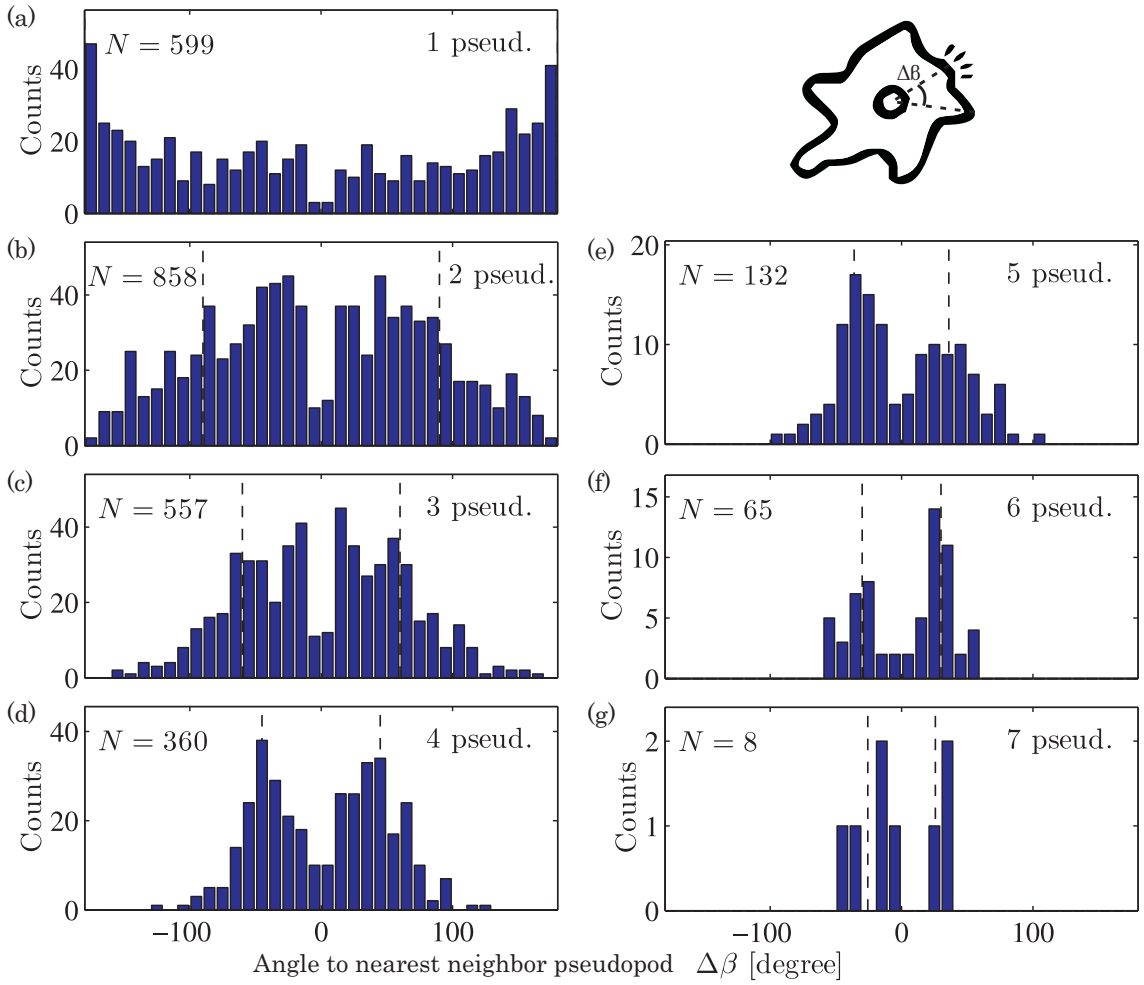

FIG. S7: The angle $\Delta\beta$ between a newly formed pseudopod and the closest neighbor pseudopod, grouped based on the number of pseudopodia of the current cell. The distribution means and peaks correlate with the angular distance $\pm 360^\circ/(2\,\nu)$ expected for pseudopodia randomly distributed along the perimeter and marked by the dashed lines in the figures. In each panel, N marks the number of pseudopodia making up the distribution. (a) Cells with $\nu = 1$ existing pseudopod ($360^\circ/2 = 180^\circ$ and coincide with the figure bounding box), (b) cells with $\nu = 2$, (c) cells with $\nu = 3$, (d) cells with $\nu = 4$, (e) cells with $\nu = 5$, (f) cells with $\nu = 6$ and (g) cells with $\nu = 7$ existing pseudopodia.

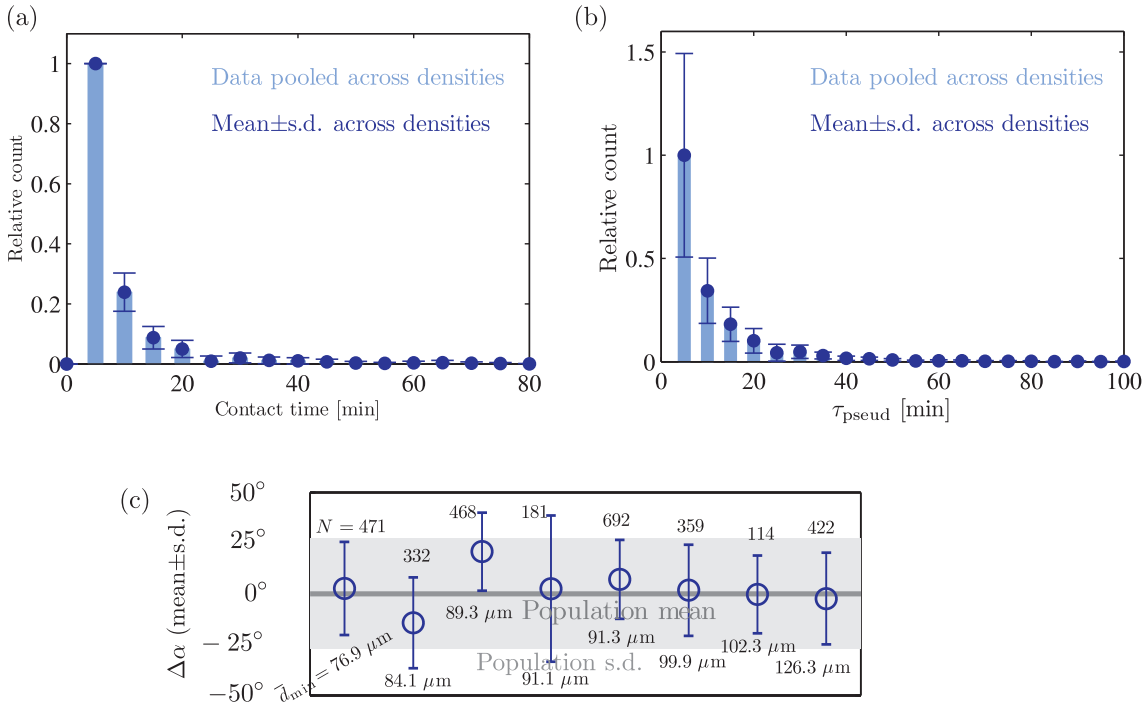

FIG. S8: Key pseudopod statistics are independent of cell density. (a) Duration of cell-cell contact time during collision. The light blue shows the pooled data given in Fig. 2(i) normalized by the largest bin count, and the darker blue filled circles are the averages across 34 independent experiments across densities (mean±s.d.). The very good agreement between the mean across densities and the pooled data, along with the small standard deviations, indicate the independence of cell density. (b) Distribution of pseudopod life times (compare to Fig. S6(a)) normalized similar to panel (a) and with light blue corresponding to pooled data across densities and darker blue to averages (mean±s.d.) from 8 independent experiments across densities. The agreement between the averages across densities and the pooled data, and the small errors again indicate an independence of this statistics on cell density. (c) Dependence on cell density of the angle $\Delta\alpha$ (compare to Fig. 2(j)) of pseudopod formation relative to the current direction of motion. The chamber density (expressed in terms of $\overline{d}_{\mathrm{min}}$) and the number of investigated pseudopodia N is listed for each data point. A symmetric distribution favoring small angles is found at all densities (see Fig. 2(j) in the main text) which at all instants is well fitted by a Gaussian plus a constant baseline. This figure illustrates the mean and standard deviation of the Gaussian term across cell densities, and illustrates that there is no dependence of cell density. The dark grey line is the population mean across densities and the light gray region indicates the corresponding standard deviation (taken from a similar fit to the data in the main panel of Fig. 2(j)).

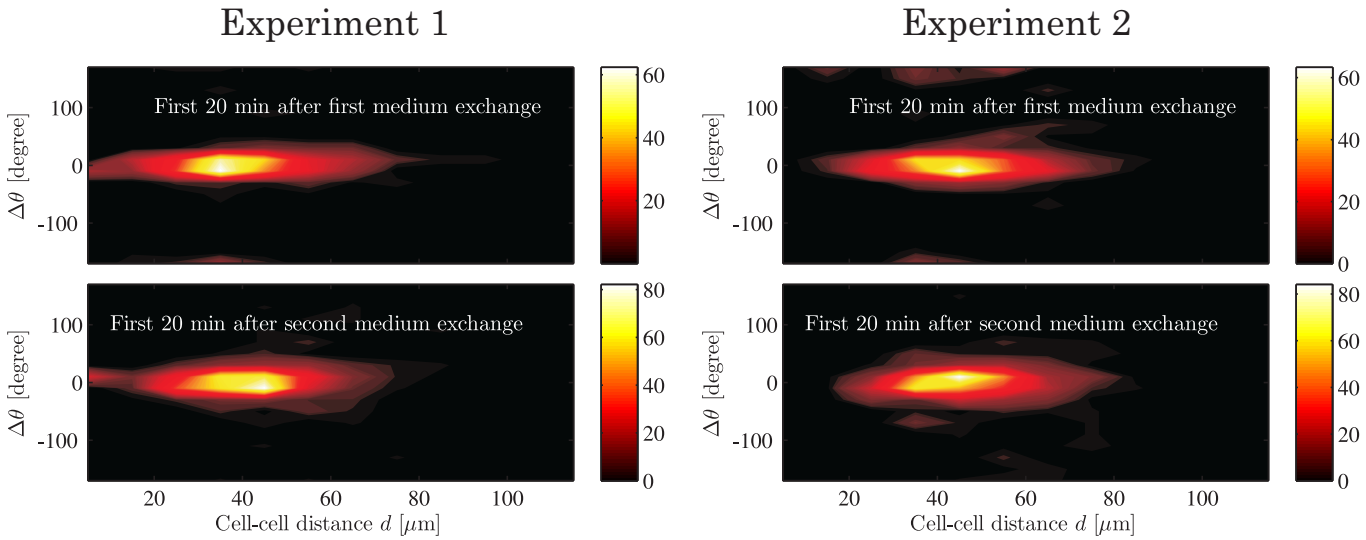

FIG. S9: Supporting experimental evidence for the existence of a cell-secreted pseudopod-inducing chemokine. The heat maps show histograms of the distances d and angle of pseudopod formation $\Delta\theta$ relative to the nearest neighbor cell (see explanatory schematic in Fig. 2(k)) during 20 min segments following media replacement for two independent experiments (shown in separate columns) with complete media replacement every two hours, with light colors corresponding to high counts and dark colors to low counts. The top row shows the result for following the first media replacement, and the bottom row the results following the second replacement, and for all cases the pseudopodia are distributed about $\Delta\theta = 0$ (similar to Fig. 2(k)), as we would expect for a cell-secreted pseudopod-inducing chemokine.

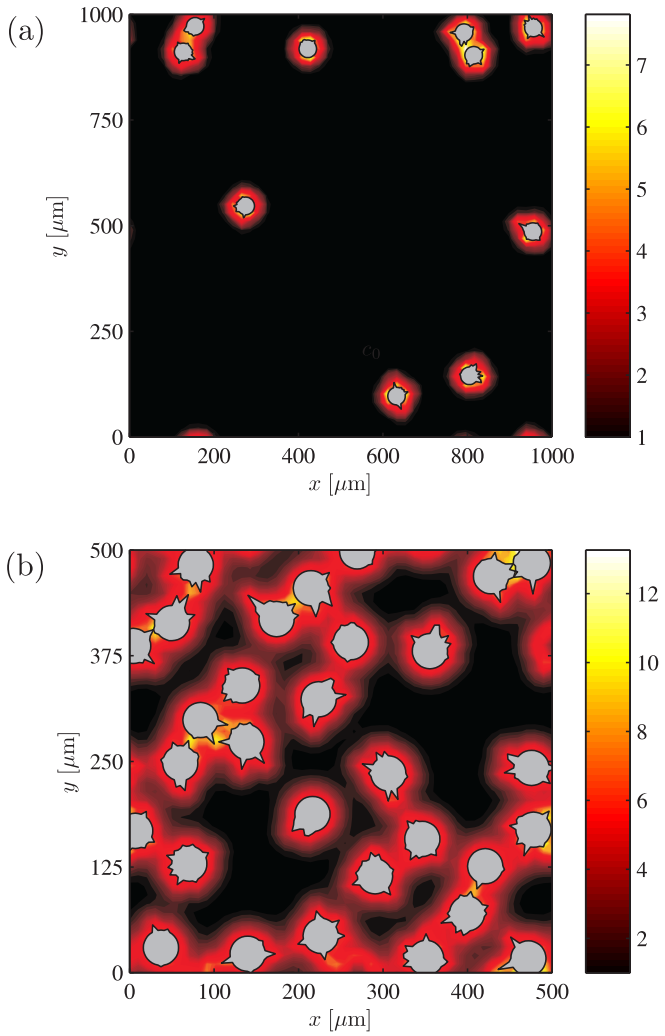

FIG. S10: Supplementary model predicted instantaneous chemokine results not shown in the main text. (a) Instantaneous chemokine concentration field from a low-density simulation. (b) Predicted chemokine concentration field taken from the same numerical experiment as shown in Fig. 3(b) and (d)-(g) in the main text.

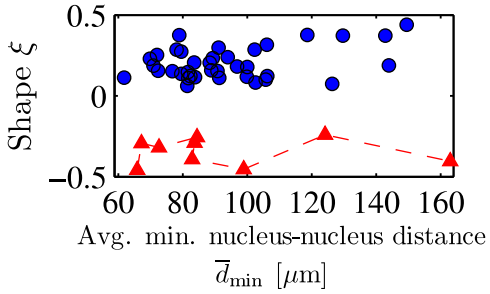

FIG. S11: Supplementary model speed distribution fit (red triangles) to experimental data (blue circles) of the shape parameter ξ of a generalized extreme value distribution across densities. Location parameter m and scale parameter s of the same fits are given in Fig. 3(i) in the main text.

III. MODEL DETAILS

The model was developed to aid in the interpretation of our experimental findings, and it was therefore crucial to construct a physically transparent model. The basic premise of the model is therefore, that each cell can be evaluated by Newtonian mechanics, as long as one is careful in the implementation of the collisions and pseudopodia traction forces. Thus our model, which can be considered as an extension of the Vicsek model [21–23], not only exploits known cellular biophysics in a direct and intuitive way contrary to the abstract thermodynamic ensemble averages of cellular Potts-type models [24, 25], but also enables handling of the few hundreds of cells per experiments - a mesoscale not suitable for continuum modeling theory [26–28].

The model cells are two-dimensional idealizations consisting of a set of N_m points discretizing the cell membrane, which are connected through a center of mass. The motion of this center of mass is taken as the motion of the cell, with the membrane points each being allowed to move in relation to the center of mass, in response to pseudopod formation or collapse, cell-cell contact, etc., as detailed in the following. The model assumes that each cell secretes chemokines, which all other cells react to. Cellular force transduction is achieved by forming pseudopodia through membrane point activation, and these form preferentially in regions of high chemokine concentration and in the current direction of motion; the former is achieved by biasing the probability of formation with the local chemokine concentration.

The model contains a list of parameters, which in most cases are determined directly from the experimental data (parameters summarized in Table S4). Whenever possible, the simplest reasonable approach has been applied, and Table S3 lists all assumptions underlying the model. The model has been implemented in MATLAB and this implementation is freely available for download at `http://sourceforge.net/projects/cell-migration/`. The flow of the program at each time step is as follows, with each part to be described in detail in the following

1. Activation of membrane points and pseudopod growth for each cell. The time since membrane point activation and pseudopod lengths are updated. This is detailed in Sec. III B.

2. Handle collisions (Sec. III E): membrane points of different cells within a distance ϵ of each other are considered to be in collision. Time since initial collision is tracked, and if the experimentally determined collision time τ_c is surpassed, the point is flagged for collapse.

3. Forces are assigned to all active points along the appropriate directions, as described by Eq. (S13) of Sec. III B 4.

4. Move all non-active points by Eq. (S17) of Sec. III C. This also includes points which are retracting following activation or collision.

5. Collapse retracting points according to Eq. (S12) of Sec. III B 3. If a membrane point has fully retracted and the waiting time τ_rest has passed, the point is transferred to a normal passive point.

6. Update time stamp and concentration field due to the new cell positions, by summing Eq. (S18) of Sec. III D for all cells.

Note that protruding points are moved before the entire cell, while retracting points first move with the cell center of mass and then retracts.

The simulation time step Δt must be smaller than all the model time scales. In addition, the time scale must also allow for colliding cells to be within ϵ of each other before the unphysical process of crossing into each other. To satisfy these criteria we have taken $\Delta t = 0.25$ min.

A. Model cell

Each cell is modeled as a set of N_m points along the cell membrane, see Fig. 3(a) in the main text, some being active and the rest passive. In a given time step, a number of the points are selected (see below) to be active and are moved outwards from the otherwise circular cell. These points thereby form pseudopodia, and their positions dictate the direction of the cell motion.

The membrane points are connected through a "cell center" with position $\mathbf{x}_\mathrm{c}$: A constant force of magnitude F_o is assigned to each active point (described below), and the cell center is displaced a distance $\Delta\mathbf{x}$ in response to the resultant force on all membrane points, see Eq. (S17). All passive points undergo the same displacement $\Delta\mathbf{x}$ (active points have already been moved). Hence, the cell motion is not an independent variable.

The cell is initially modeled as a sphere with radius $r = 20.9$ μm corresponding to the mean radius of the cells in the experiments, see Fig. S12(a). The real cells are obviously not circular, but as time passes, the formation and collapse of pseudopodia make the model cell shape a dynamic and dependent entity, in agreement with experimental observation. The pseudopod width w is taken from the data to be 8 μm (Fig. S12(b)), which agrees with the report of pseudopod width of ∼5 μm in [9]. The number of membrane points per cell N_m is therefore taken as the cell circumference divided by twice the pseudopod width (by extending a membrane point, the model base pseudopod width is roughly twice the distance between two membrane points),

$$N_\mathrm{m} = \frac{2\pi r}{2w} \approx 36. \tag{S9}$$

If two neighboring points are activated at the same time, the width of the pseudopod becomes larger and the force in this direction increases, since each of the

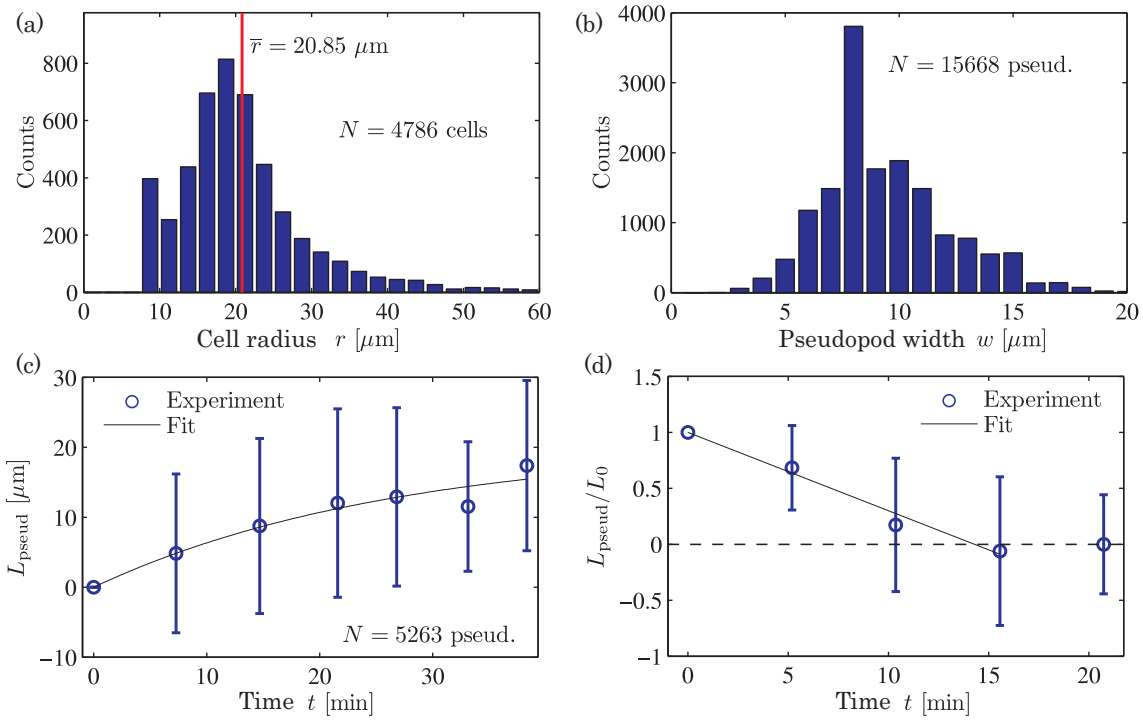

FIG. S12: Experimental determination of model parameters. (a) Cell radius is computed as the average distance between the nucleus and the cell outline. (b) Pseudopod width has been measured at the base of the protrusion. (c) Pseudopod growth obtained from 5263 pseudopodia is approximated by an exponential function (Eq. (S10)). (d) Pseudopod collapse following cessation of a pseudopod from either age or contact with other cells occurs at a constant rate depending on the initial length. Pseudopodia do not collapse between the second to last and final data points (at $t = 16$ min and $t = 22$ min).

two activated points of course pull with the same force F_{o}. This is in agreement with experimental work on the distribution of a cytosolic kinase (PI3K) known to be involved in the polymerization of actin, which has revealed localized and independent signaling domains of the size of small pseudopodia in the wider pseudopodia known as lamellipodia [9].

It was found experimentally that the number of pseudopodia per cell varies about a constant value, ν_{m}, which was found to be in the range $1 - 7$ (see Fig. 2(c) in the main text). To account for this in the model, each cell is assumed to have a constant number of pseudopodia N_{p}, so a pseudopod cannot form before an old one stops due to either age or contact with another cell (detailed below). However, since it takes some time for a former pseudopod to retract back into the cell, there will be times where the model cell will appear to have more pseudopodia than N_{p}; likewise, cells which often collide with other cells will at some instances appear to have fewer pseudopodia. Each model cell is a random number of pseudopodia N_{p} ranging from 1 to 7 which does not change. We find no difference whether each cell is assigned N_{p} according to the distribution shown in Fig. 2(c) in the main text or from a uniform distribution, so to limit the number of variables we have drawn N_{p} from a uniform distribution for all results.

Experimental studies of isolated migrating cells have revealed that they have a protrusion opposite the direction of motion in addition to their pseudopodia. This protrusion, also known as the uropod, is pulled towards the cell center by intracellular myosin, while applying less traction force than pseudopodia [29]. Contrary to these findings, most cells in our experiments did not exhibit an observable morphological polarity as they formed pseudopodia in almost any direction, and consequently uropodia could rarely be unambiguously identified. In addition, the dynamics of uropod formation and maintenance for a cell which is constantly changing direction of motion is not well understood, and fibroblasts in particular have lower levels of uropodial myosin compared to e.g. *Dictyostelium* cells. In the experimental observations on which we base our model we therefore neglected cell uropodia, and all experimentally observed protrusions were treated as pseudopodia. Due to the comparatively small traction forces applied by the uropodia and their low numbers, this is a reasonable first approximation, and the good agreement between model and experiment further justify these assumptions.

B. Pseudopod dynamics

Pseudopod growth and collapse are complex processes at the molecular level which have been investigated for

decades [29–31]. The focus of the current work is on modeling the motile behavior at the cell-level, so pseudopod growth and collapse are measured from the data and used as input to the model.

1. Life of a pseudopod

We found experimentally that the number of pseudopodia is roughly constant per cell during an experiment, but with a varying life times (Fig. S6(a)). In the model each pseudopod is assigned a life time drawn from the distribution given in Fig. S6(c). Since we find that the variation in the number of pseudopodia about $\nu_{\rm m}$ is low, a new point is activated only when an old one exists longer than the prescribed life time. When this happens, all non-active and non-collided points are assigned a probability of pseudopod formation (details given below), and for each ending pseudopod a new is picked randomly from the pool of available membrane points. Hence, the number of activated points is conserved but the number of pseudopodia will change as new pseudopodia form while ending pseudopodia retract (pseudopod collapse described in detail below).

Following collision of a pseudopod with another cell, it is observed that a new pseudopod does not form at the position of the old pseudopod immediately after the release. This is in line with biochemical investigations which indicate that contact inhibition of locomotion is caused by a local inhibition of actin polymerization in the region of contact [32]. This is implemented in the model by including a resting time $\tau_{\rm rest}$ following the release of the collided points, where said point cannot be reactivated. Following the data, we pick $\tau_{\rm rest} = 5.5$ min, the mean time difference between two frames.

2. Protrusion

For each activated point, pseudopod protrusion is modeled by moving the point radially outward. We followed the tip of 5263 pseudopodia experimentally to obtain data on the growth of the pseudopodia The data shows (Fig. S12(c)) that the protrusion (pseudopod) length $L_{\rm pseud}(t)$ as a function of time can be approximated by

$$L_{\rm pseud}(t) = L_0 \left(1 - {\rm e}^{-t/\tau_{\rm pseud}^{\rm growth}}\right), \tag{S10}$$

with $L_0 = 26.7$ μm and $\tau_{\rm pseud}^{\rm growth} = 20.2$ min.

There are large variations in pseudopod lengths (hence the large errorbars in Fig. S12(c)), but aiming for simplicity only the mean is used in the model.

The mathematical formulation for the protrusion of an activated point at position $\mathbf{x}_i$ at a time t during the growth of the pseudopod is

$$\mathbf{x}_i + L_{\rm pseud}(t) \frac{\mathbf{x}_i + \mathbf{x}_{\rm c}}{|\mathbf{x}_i + \mathbf{x}_{\rm c}|}, \tag{S11}$$

where $\mathbf{x}_{\rm c}$ is the position of the cell center.

3. Collapse

After the prescribed pseudopod life time has passed since activation, pseudopodia collapse back into the cell. Biophysically this occurs since the cell-substrate adhesion is broken and the cell degrades the polymerized actin, so pseudopod retraction is caused by the elastic force of the membrane. The data shows (Fig. S12(d)) that the collapse rate depends on pseudopod length, since the normalized pseudopod length may be fitted by

$$\frac{L_{\rm pseud}(t)}{L_0} = -K\, t, \tag{S12}$$

with collapse rate $K = 0.07$ min^{-1}. Hence, in the model each collapsing membrane point does so an amount $K\, L_0\, \Delta t$ per time step, where L_0 is the full length of the pseudopod from Eq. (S10) and Δt is the duration of the time step. Similar to pseudopod extension, collapse of a point occurs along the direction from the nucleus to the point. As shown in Fig. S12(d), the average pseudopod has completely retracted after ~ 16 min, and therefore does not retract any further; hence the second to last and last data points have about the same length. The fit presented by Eq. (S12) only applies until the pseudopod has collapsed, so in the model we retract pseudopodia only until the reach the radius $\overline{r}$ of the unperturbed cell.

A collapsing point is first moved along with the rest of the cell before the collapse is invoked. Collapsing points may be activated in later time steps, in which case the point transitions to an activated point and the cycle restarts.

4. Pseudopod force

The force assigned to each activated point is a consequence of the attachment and subsequent pulling of microtubules on the adhesion made by the cell with the substrate at the base of the pseudopod. Microtubules constantly "feel out" the inside of the cell but the formation of the attachment depends on the proximity of the nearest microtubule and the pulling force obviously scales with the number of microtubules that attach to each adhesion. However, the microtubules emanate from the centrosome, which is found right in front of the nucleus even for migrating cells, so the direction of the force can be approximated by the pseudopod-nucleus direction [18, 33]. Furthermore, relative variations of the pseudopod point forces are on the order $\sim$2 both within the individual cell and between cells [19], and locally the force is more likely to be applied in short bursts of much smaller spatial extend than the width of the pseudopod [9].

Due to their relative small size and aiming for simplicity, these variations are ignored, so each active point is

assigned a force of magnitude F_o along the direction from the cell center to the activated point i

$$\mathbf{F}_i = F_\mathrm{o}\frac{\mathbf{x}_i + \mathbf{x}_\mathrm{c}}{|\mathbf{x}_i + \mathbf{x}_\mathrm{c}|}, \tag{S13}$$

where as in Eq. (S11) $\mathbf{x}_i$ is the position of the ith point and $\mathbf{x}_\mathrm{c}$ is the position of the cell center. The point force at the base of each pseudopod is estimated to $F_\mathrm{o} \approx 1.1 \times 10^{-7}$ N from Munevar *et al.* [19] who showed experimentally that traction forces can be well approximated by point forces at the pseudopodia in NIH 3T3 fibroblasts.

5. *Pseudopod formation bias*

A new membrane point is activated after an already active point exceeds its life time or collides with another cell. The stochastic selection of this new point i is biased by secreted chemokine with factor Π_i^c and the current direction of motion with factor Π_i^d, so the probability that this point is activated out of the total N_m points of the cell is

$$p_i = \frac{\Pi_i^c + \Pi_i^d}{\sum_{i=1}^{N_\mathrm{m}}(\Pi_i^c + \Pi_i^d)}. \tag{S14}$$

A biased stochastic activation was used due to the low number of involved intra- and extracellular signaling molecules (at typical extracellular chemokine concentrations in the nanomolar range [34, 35] there are large relative fluctuations of as much as 100 % [36]).

The directional bias is determined from a fit to the experimental data in Fig. 2(j) using the angle $\Delta\alpha$ between the current direction of motion and the line connecting the center-of-mass $\vec{x}_\mathrm{c}$ and the current membrane point. A Gaussian fit to the normalized experimental data $\Pi_i^\mathrm{d}(\Delta\alpha) = A\,\mathrm{e}^{\frac{-\Delta\alpha^2}{2\,a^2}}$ with mean 0°, standard deviation $a = 29.7°$, and amplitude $A = 0.05$ was used.

Our experimental observations only imply the existence of a pseudopod formation bias by cell-secreted chemokines, not the exact form. To implement this crucial feature in the model, we therefore used previously published results on single-cell chemotaxis. Firstly, the results of Arriemerlou and Meyer implied that pseudopods are more likely to form in the regions of higher chemokine concentration [9]. Secondly, the previously mentioned results from single-cell experiments on NIH 3T3 fibroblasts by Melvin *et al.* had revealed that relative concentration gradients $(\Delta c/\Delta x)/c_0$ of 0.002 µm^{-1} are required for unambiguous chemotactic response, and that the response saturates at higher concentrations, while relative concentrations lower than the aforementioned limit do not produce reliable chemotaxis [10]. Furthermore, it has been demonstrated that the local gradient across the cell relative to the average concentration of the cell is the decisive parameter [34]. All this points to a sigmoidal activation function based on local relative chemokine concentration. We use a Hill function based on the local relative chemokine concentration of the cell at membrane point i, $c_i/\overline{c}$, where $\overline{c} = \sum_{i=1}^{N_\mathrm{m}} c_i/N_\mathrm{m}$ is the instantaneous average concentration experienced by the cell, as sigmoidal functions of this type are ubiquitous in biochemical signaling activation including gradient sensing in bacterial chemotaxis [37]. The biasing function is

$$\Pi_i^\mathrm{c} = \frac{\left(\frac{c_i}{\overline{c}}\right)^h}{1 + \left(\frac{c_i}{\overline{c}}\right)^h}, \tag{S15}$$

where h is the Hill coefficient.

Running our model for isolated cells, we found we could reproduce the experimental results of [10] using $h = 20$ in Eq. (S15), see Fig. 3(c) where each data point represents the average over 20 single-cell simulations each run for 300 min at each concentration. Biochemically, the Hill coefficient h is an expression of cooperativity among the chemical receptors mediating the chemotactic signal, with the coefficient corresponding to the number of cooperating receptors, and it has been shown that improved gradient sensing is achieved by increasing the cooperativity [38]. While the value $h = 50$ used in the model is unrealistically high — the reference value is $h \approx 3$ found for haemoglobin [39] — Hill coefficients of ∼10 have been reported for bacterial chemotaxis [37], and Hill-like behavior with apparent Hill coefficients of $h \approx 42$ have furthermore been demonstrated to arise from more complex interlinked signaling networks in the maturation of *Xenopus laevis* oocytes [40].

TABLE S3: Model assumptions

– Cell motion is quasi-static
– The scale of secreted concentration is the same for all cells, c_0
– All pseudopodia apply a force of the same magnitude, F_o
– All collisions last the same time, τ_c
– Chemokine activation of membrane points is biased by a Hill function of the relative concentration. This function is the same for all membrane points and all cells.
– All cells have the same friction parameter γ
– All pseudopodia grow and collapse according to the same relations, Eqs. (SS10) and (SS12)
– All cells are circular with the same radius $\overline{r}$
– Each cell has a fixed number of pseudopods at each time, but different cells have different numbers

C. Cell motion

Having activated and protruded the appropriate points and assigned forces to them, the resulting force on the cell is used to compute the cell velocity. Due to the timescales and small masses involved, cell inertia is negligible

TABLE S4: Model assumptions and values assigned to model parameters.

Parameter	Symbol	Value and unit	Source
Cell friction	γ	39.0 kg s^{-1}	Global fit
Pseudopod force	F_o	1.1×10^{-7} N	Extracted from Munevar *et al.* [19]
Number of membrane points per cell	N_m	36	Eq. S9 and Fig. S12(a)
Number of pseudopodia per cell	N_p	$1-7$	Fig. 3(c) in the main text
Full pseudopod length	L_0	26.7 µm	Eq. (S10) and Fig. S12(c)
Pseudopod collapse rate	K	0.07 min^{-1}	Eq. (S12) and Fig. S12(d)
Hill coefficient	h	20	Fig. 3(c) in the main text and Melvin *et al.* [10]
Decay length scale of secreted chemokines	ℓ_{diff}	340 µm	Fig. S12(a), combined with Francis and Palsson [41]
Cell radius	r	20.9 µm	Fig. S12(a)
Collision tolerance distance	ϵ	3 µm	Chosen to best capture the dynamics, no observable changes choosing ϵ in the range 1 µm − 5 µm
Cell-cell contact time	τ_c	5.5 min	Fig. S12(e)
Time between successive activations of the same membrane point	τ_{rest}	5.5 min	Own data
Characteristic pseudopod growth time	τ_{pseud}^{growth}	20.7 min	Eq. (S10) and Fig. S12(c)

and the following relationship is postulated

$$\sum_i \mathbf{F}_i = \gamma\, \mathbf{v}, \tag{S16}$$

where γ is a constant and $\mathbf{v}$ is the velocity of the cell. Physically, γ accounts for the Stokes drag from the fluid and the cell friction force with the substrate, which also scales linearly with the velocity. γ is the same for all cells and is fitted from the data at the value $\gamma = 39.0$ kg s^{-1}, which compares reasonably well with an estimated friction coefficient of $\gamma \approx 29$ kg s^{-1} from Munevar *et al.* [19] and an order-of-magnitude estimate of the friction per unit cell surface area of 10^9 kg s^{-1} m^{-2} by Larripa and Mogilner [20]. The displacement of the model cell center $\Delta\mathbf{x}$ is then given by

$$\Delta\mathbf{x} = \mathbf{v}\,\Delta t, \tag{S17}$$

where Δt is the time step. It has been shown in the literature that NIH 3T3 fibroblasts move along the direction of the resulting traction force [19], which essentially is the postulate of Eqs. (S16) and (S17). All points not activated are moved similarly to the cell center (the activated points have already been moved).

D. Secretion of signaling molecules

To mediate the chemotactic response of Fig. 3(e), model cells secrete chemokines. We assume that each model cell secretes at a constant rate Γ from the entire perimeter and the concentration field from each cell is thus approximated by the analytical solution for a constant source (see e.g. [41])

$$c(d) = G\frac{r}{d-r}\frac{\ell_{diff}}{\sqrt{\pi}}\left[\mathrm{e}^{-\frac{(d-2r)^2}{\ell_{diff}^2}} - \mathrm{e}^{-\frac{d^2}{\ell_{diff}^2}} - \frac{|d-2r|}{\frac{\ell_{diff}}{\sqrt{\pi}}}\mathrm{erfc}\left(\frac{|d-2r|}{\ell_{diff}}\right) + \frac{d}{\frac{\ell_{diff}}{\sqrt{\pi}}}\mathrm{erfc}\left(\frac{d}{\ell_{diff}}\right)\right], \tag{S18}$$

where $\mathrm{erfc}(x)$ is the complementary error function, d is the distance from an extracellular point to the cell membrane, r is the cell radius, $G = \Gamma/(2D)$ is the concentration gradient at the cell membrane (taken to be the same for all cells; D is the diffusivity of the chemokine) and ℓ_{diff} is the length scale the concentration field decays on. Due to dilution and degradation, the effective signaling distance of a cell is estimated to 50 times the cell radius by Francis and Paulsson [41], and the length scale ℓ_{diff} is therefore taken to be 1/3 of the effective signaling distance of a cell of radius $r \approx 20$µm, i.e. $\ell_{diff} = 340$ µm. Assuming the rate of chemokine secretion is one order of magnitude lower than the rate of antibody production we pick $\Gamma = 100$ molecule per cell per second [42] and since furthermore $D = 10^{-10}$ m^2 s^{-1} we find $G = 6.6 \times 10^{-4}$ mol m^{-4}.

E. Cell-cell contact

The contact inhibition of locomotion is characterized by the time of contact τ_c (Fig. 2(i) in the main text). Aiming for simplicity we assume in the model that the force is applied until the contact stops. The contact time τ_c is taken as the most frequent experimentally observed

contact time of pseudopodia in contact with other cells from the data, which unfortunately is identical to the mean sampling time $\Delta t_{\rm samp}$,

$$\tau_{\rm c} = 5.5 \text{ min.} \tag{S19}$$

The contact inhibition is implemented at the activation point level. If a point comes within a distance ϵ of any point of any other cell (does not need to be an activated point) the two points are deemed to be in contact. This continues until a total of $\tau_{\rm c}$ has passed since the initial contact, and the local force is stopped. Hereafter the points transition to the normal collapse routine, in accordance with the experimental observations. The exact value of ϵ does not influence the behavior of the model cells for the range $1 - 5$ μm.

F. Summary of model parameters

The parameters of the model are summarized in Table S4. There is one fit (the friction coefficient γ, a global fit) while the rest of the parameters are obtained directly from the data or the literature.

G. Boundary conditions

In the experiments we only track cells in the middle of the chamber, neglecting cells close to the wall. In the model we imposed these boundary conditions in two different ways: (*i*) applying periodic boundary conditions on the secreted chemokine fields and cell motion, or (*ii*) including cells around the cells on interest (in a band of 4-5 cells) and include a density-specific background chemokine concentration representing the almost constant concentration field experienced by the cells. We found no detectable difference in the outcome, but using periodic boundary conditions saves computational time and therefore speeds up the numerical analysis. Consequently, all results presented in the paper have been computed using these boundary conditions.

H. Model output and comparison to experiment

We initiate the model by seeding cells at a desired concentration, using either the known starting positions from an experiment or random placement. We store the positions of the model cells and the concentration field at each time step, yielding trajectories as shown in Fig. 3(b) in the main text and concentration fields as shown in Fig. S10. For true comparison between model and experimental data, the model trajectories are sampled at the experimental sampling rate, and motility statistics are computed from these resampled data. Furthermore, the first 20 min of the experimental data is discarded for these comparisons due to the significant chemotactic response caused by the low background level during these times. The model predictions are compared to experiments in Fig. 3 in the main text.

The numerical implementation of the model is not parallellized, so running the program becomes increasingly time consuming with the addition of more cells. To circumvent this issue, we ran several numerical experiments at the same cell density in parallel using $\sim$ 30 cells in each, and then averaged over all cells in all experiments to extract distributions of single-cell speed, directional autocorrelation and maximum path distance. The outcome of this cost and time-reduced simulation scheme was compared to simulations using $\sim$ 100 cells in two cases, where no variations exceeding those of finite statistics where detected.

I. Model outlook

Our statistical results combined with the model could be used to derive a continuum theory of the collective migration. While the number of cells in our experiment (a few hundred) is typically too low for a continuum description, it would be of great interest to derive such a theory for future macroscale studies. Such continuum theories have successfully been applied to collective behavior of both swimming and migrating cells [26–28]. Our experimentally validated model could be used to derive a continuum theory of the collective migration, which we would expect to include pair correlations due to the importance of cell-cell interactions in shaping local dynamics, much like the Zimm theory of polymers in dilute solutions [43]. Specifically, obtaining a sound description of the "collision" term of the continuum theory based on the microscopic (subcellular) dynamics described in our paper would not only contribute to the identification of the correct continuum model (in contrast to ad-hoc arguments and empirical data fitting), but would also lead to a deeper understanding of collective dynamics and rheology.

[1] Lee, T. K, Denny, E. M, Sanghvi, J. C, Gaston, J. E, Maynard, N. D, Hughey, J. J, & Covert, M. W. (2009) A noisy paracrine signal determines the cellular NF-κB response to lipopolysaccharide. *Sci. Signal.* **2**, 93.

[2] Selmeczi, D, Mosler, S, Hagedorn, P. H, Larsen, N. B, & Flyvbjerg, H. (2005) Cell motility as persistent random motion: Theories from experiments. *Biophys. J.* **89**, 912–931.

[3] Gómez-Sjöberg, R, Leyrat, A. A, Pirone, D. M, Chen, C. S, & Quake, S. R. (2007) Versatile, fully automated,

microfluidic cell culture system. *Anal. Chem.* **79**, 8557–8563.

[4] Tay, S, Hughey, J. J, Lee, T. K, Lipniacki, T, Quake, S. R, & Covert, M. W. (2010) Single-cell NF-κB dynamics reveal digital activation and analogue information processing. *Nature* **466**, 267–271.

[5] Li, L, Cox, E. C, & Flyvbjerg, H. (2011) "Dicty dynamics": Dictyostelium motility as persistent random motion. *Phys. Biol.* **8**, 046006.

[6] Bosgraaf, L & van Haastert, P. J. M. (2010) Quimp3, an automated pseudopod-tracking algorithm. *Cell Adh. Migr.* **4**, 46–55.

[7] Trepat, X, Wasserman, M. R, Angelini, T. E, Millet, E, Weitz, D. A, Butler, J. P, & Fredberg, J. J. (2009) Physical forces during collective cell migration. *Nat. Phys.* **5**, 426–430.

[8] Andrew, N & Insall, R. H. (2007) Chemotaxis in shallow gradients is mediated independently of PtdIns 3-kinase by biased choices between random protrusions. *Nature Cell Bio.* **9**, 193–200.

[9] Arrieumerlou, C & Meyer, T. (2005) A local coupling model and compass parameter for chemotaxis. *Dev. Cell* **8**, 215–227.

[10] Melvin, A. T, Welf, E. S, Wang, Y, Irvine, D. J, & Haugh, J. M. (2011) In chemotaxing fibroblasts, both high-fidelity and weakly biased cell movements track the localization of PI3K signaling. *Biophys. J.* **100**, 1893–1901.

[11] Seppä, H, Grotendorst, G, Seppä, S, Schiffmann, E, & Martin, G. R. (1982) Platelet-derived growth factor is chemotactic for fibroblasts. *J. Cell Bio.* **92**, 584–588.

[12] Postlethwaite, A. E, Keski-Oja, J, Moses, H. L, & Kang, A. H. (1987) Stimulation of the chemotactic migration of human fibroblasts by transforming growth factor β. *J. Exp. Med.* **165**, 251–256.

[13] Kanazawa, S, Fujiwara, T, Matsuzaki, S, Shingaki, K, Taniguchi, M, Miyata, S, Tohyama, M, Sakai, Y, Yano, K, Hosokawa, K, & Kubo, T. (2010) bFGF regulates PI3-kinase-Rac1-JNK pathway and promotes fibroblast migration in wound healing. *PLoS One* **5**, e12228.

[14] Silzle, T, Kreutz, M, Dobler, M. A, Brockhoff, G, Knuechel, R, & Kunz-Schughart, L. A. (2003) Tumor-associated fibroblasts recruit blood monocytes into tumor tissue. *Eur. J. Immunol.* **33**, 1311–1320.

[15] Rojas-Valencia, L, Montiel, F, no, M. M, Selman, M, & Pardo, A. (1995) Expression of a 2.8-kb PDGF-B/c-sis transcript and synthesis of PDGF-like protein by human lung fibroblasts. *Chest* **108**, 240–245.

[16] Mansbridge, J. N, Liu, K, Pinney, R. E, Patch, R, Ratcliffe, A, & Naughton, G. K. (1999) Growth factors secreted by fibroblasts: role in healing diabetic foot ulcers. *Diabetes, Obesity and Metabolism* **1**, 265–279.

[17] Smith, R. S, Smith, T. J, Blieden, T. M, & Phipps, R. P. (1997) Fibroblasts as sentinel cells. Synthesis of chemokines and regulation of inflammation. *Am. J. Pathol.* **151**, 317–322.

[18] Alberts, B, Johnson, A, Lewis, J, Raff, M, Roberts, K, & Walter, P. (2007) *Molecular biology of the cell.* (Garland Science, New York), 5th edition.

[19] Munevar, S, Wang, Y, & Dembo, M. (2001) Traction force microscopy of migrating normal and H-ras transformed 3T3 fibroblasts. *Biophys. J.* **80**, 1744–1757.

[20] Larripa, K & Mogilner, A. (2006) Transport of a 1D viscoelastic actin-myosin strip of gel as a model of a crawling cell. *Physica A* **372**, 113–123.

[21] Vicsek, T, Czirók, A, Ben-Jacob, E, Cohen, I, & Shochet, O. (1995) Novel type of phase transition in a system of self-driven particles. *Phys. Rev. Lett.* **75**, 1226–1229.

[22] Szabó, B, Szöllösi, G. J, Gönci, B, Jurányi, Z, Selmeczi, D, & Vicsek, T. (2006) Phase transition in the collective migration of tissue cells: Experiment and model. *Phys. Rev. E* **74**, 061908.

[23] Yamao, M, Naoki, H, & Ishii, S. (2011) Multi-cellular logistics of collective cell migration. *PLoS One* **6**, e27950.

[24] Graner, F & Glazier, J. A. (1992) Simulation of biological cell sorting using a two-dimensional extended Potts model. *Phys. Rev. Lett.* **69**, 2013–2016.

[25] Szabó, A, Ünnep, R, Méhes, E, Twal, W. O, Argraves, W. S, Cao, Y, & Czirók, A. (2010) Collective cell motion in endothelial monolayers. *Phys. Biol.* **7**, 046007.

[26] Saintillian, D & Shelley, M. J. (2008) Instabilities and pattern formation in active particle suspensions: kinetic theory and continuum simulations. *Phys. Rev. Lett.* **100**, 178103.

[27] Lambert, G, Liao, D, & Austin, R. H. (2010) Collective escape of chemotactic swimmers through microscopic ratchets. *Phys. Rev. Lett.* **104**, 168102.

[28] Basan, M, Joanny, J.-F, Prost, J, & Risler, T. (2011) Undulation instability of epithelial tissue. *Phys. Rev. Lett.* **106**, 158101.

[29] Lauffenberger, D. A & Horwitz, A. F. (1996) Cell migration: A physically integrated molecular process. *Cell* **84**, 359–369.

[30] DiMilla, P. A, Barbee, K, & Lauffenburger, D. A. (1991) Mathematical model for the effects of adhesion and mechanics on cell migration speed. *Biophys. J.* **60**, 15–37.

[31] Schreiber, C. H, Stewart, M, & Duke, T. (2010) Simulation of cell motility that reproduces the force-velocity relationship. *Proc. Natl. Acad. Sci. USA* **107**, 9141–9146.

[32] Carmona-Fontaine, C, Matthews, H. K, Kuriyama, S, Moreno, M, Dunn, G. A, Parsons, M, Stern, C. D, & Mayor, R. (2008) Contact inhibition of locomotion *in vivo* controls neural crest directional migration. *Nature* **456**, 957–961.

[33] Ueda, M, Gräf, R, MacWilliams, H. K, Schliwa, M, & Euteneuer, U. (1997) Centrosome positioning and directionality of cell movements. *Proc. Natl. Acad. Sci. USA* **94**, 9674–9678.

[34] Fuller, D, Chen, W, Adler, M, Groisman, A, Levine, H, Rappel, W.-J, & Loomis, W. F. (2010) External and internal constraints on eukaryotic chemotaxis. *Proc. Natl. Acad. Sci. USA* **107**, 9656–9659.

[35] Haessler, U, Pisano, M, Wu, M, & Swartz, M. A. (2011) Dendritic cell chemotaxis in 3D under defined chemokine gradients reveals differential response to ligands CCL21 and CCL19. *Proc. Natl. Acad. Sci. USA* **108**, 5614–5619.

[36] Landau, L. D & Lifshitz, E. M. (1980) *Statistical Physics, Part I.* (Butterworth–Heinemann), 3rd edition.

[37] Li, G & Weis, R. M. (2000) Covalent modification regulates ligand binding to receptor complexes in the chemosensory system of *Escherichia coli. Cell* **100**, 357–365.

[38] Hu, B, Chen, W, Rappel, W.-J, & Levine, H. (2010) Physical limits to cellular sensing of spatial gradients. *Phys. Rev. Lett.* **105**, 048104.

[39] Stryer, L. (1995) *Biochemistry.* (Freeman, New York), 4th edition.

[40] Ferrell, J. E & Machleder, E. M. (1998) The biochem-

ical basis of an all-or-none cell fate switch in Xenopus oocytes. *Science* **280**, 895–898.

[41] Francis, K & Palsson, B. O. (1997) Effective intercellular communication distances are determined by the relative time constants for cyto/chemokine secretion and diffusion. *Proc. Natl. Acad. Sci. USA* **94**, 12258–12262.

[42] Savinell, J. M, Lee, G. M, & Palsson, B. O. (1989) On the orders of magnitude of epigenic dynamics and monoclonal antibody production. *Bioprocess Eng.* **4**, 231–234.

[43] Doi, M. (1995) *Introduction to polymer physics*. (Oxford University Press).

Supporting Information

Vedel et al. 10.1073/pnas.1204291110

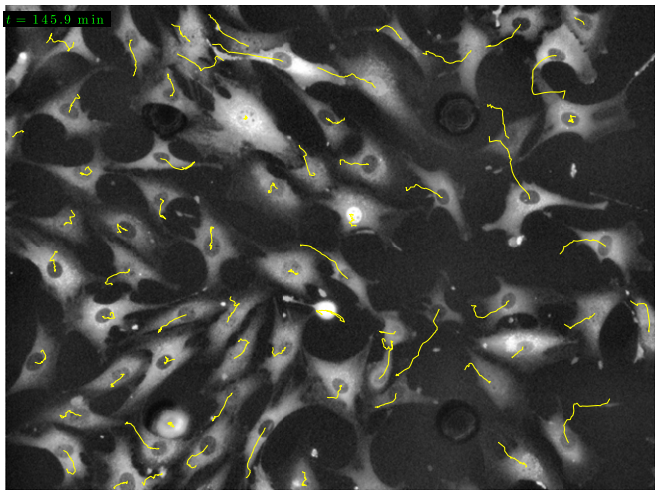

Movie S1. The movement of cells at medium density in a chamber during 200 min. The trajectories are given by yellow lines.

Movie S1

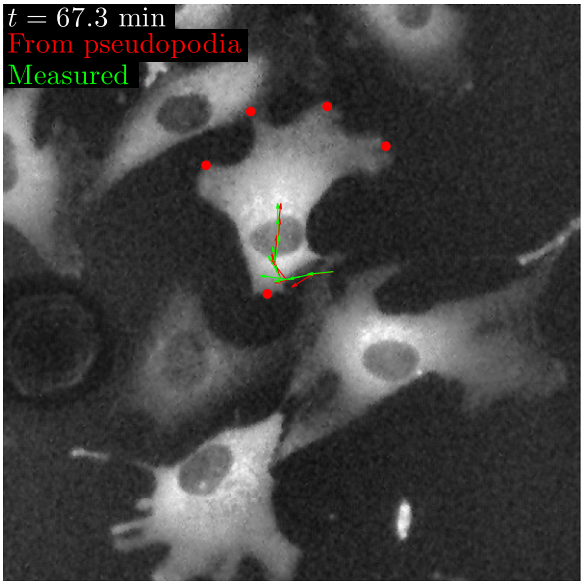

Movie S2. The positions and life times of the pseudopodia change dynamically during the course of an experiment, as illustrated for two cells. Pseudopodia are marked by red circles, with arrows indicating the actual direction of motion (green) and the direction of movement predicted from the pseudopodia (red).

Movie S2

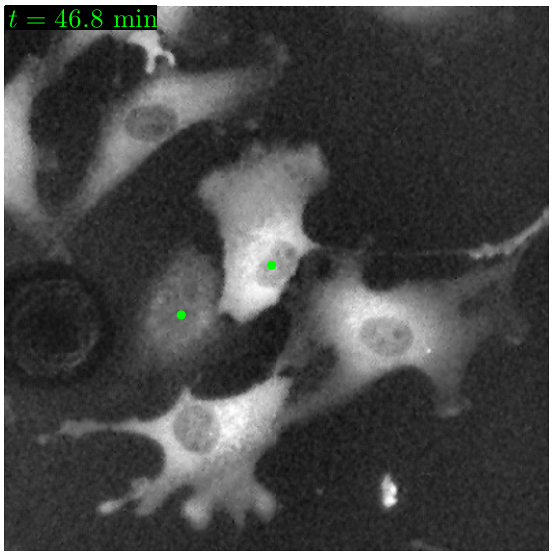

Movie S3. The cells exhibit contact inhibition of locomotion. Colliding cells (green) transiently remain in contact (for roughly 5.5 min; see Fig. 2*I*), before they move away from each other, followed by collapse of the touching pseudopodia of different cells.

Movie S3

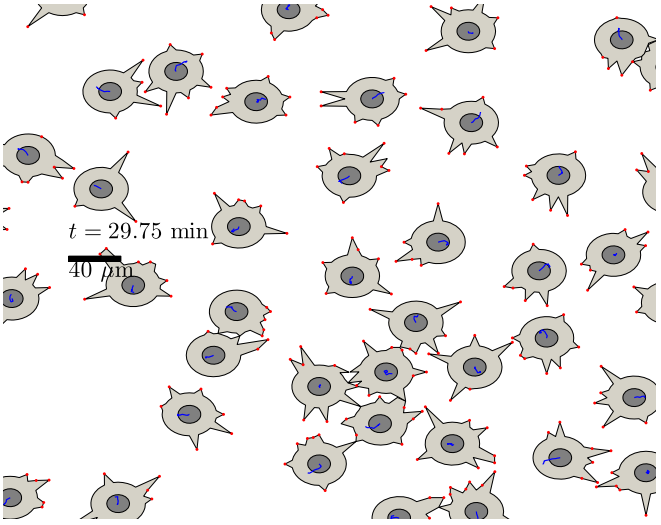

Movie S4. Illustration of model cell migration behavior. Active membrane points are indicated by red dots, and the trajectories of the cells are indicated by blue lines.

Movie S4

Other Supporting Information Files

SI Appendix (PDF)